UNIVERSITY OF OKLAHOMA

GRADUATE COLLEGE

# APPLYING THE SIMPLIFIED LOCAL DENSITY MODEL TO STUDY THE EFFECTS OF CONFINEMENT ON DENSITY IN SHALE FORMATION

A THESIS

SUBMITTED TO THE GRADUATE FACULTY

in partial fulfillment of the requirements for the

Degree of

MASTER OF SCIENCE

By

BRANDON TOLBERT
Norman, Oklahoma
2016

Downloaded from SHAREOK. Persistent Handle URL: https://hdl.handle.net/11244/44925

APPLYING THE SIMPLIFIED LOCAL DENSITY MODEL TO STUDY THE EFFECTS OF CONFINEMENT ON DENSITY IN SHALE FORMATION

A THESIS APPROVED FOR THE
MEWBOURNE SCHOOL OF PETROLEUM AND GEOLOGICAL ENGINEERING

BY

_____
Dr. Xingru Wu, Chair

_____
Dr. Ahmad Jamili

_____
Dr. Ahmad Sakhaee-Pour

© Copyright by BRANDON TOLBERT 2016
All Rights Reserved.

Dedicated to my parents and family members who have made many sacrifices to allow me to follow my dreams

## Acknowledgements

I am very appreciative to those who have driven and challenged me these past five years at the University of Oklahoma. I'm here because I am a product of a series of mentors throughout my life. Despite several obstacles and setbacks, I would not change a single thing. The guidance and support I have acquired from my professors is insurmountable. I will take what they have taught me and apply their knowledge throughout my career.

I would especially like to thank my advisor and friend, Dr. Xingru Wu. Dr. Wu exhibits a unique skill set and professionalism within the petroleum engineering spectra that I have not encountered before. With his guidance I have benefited in multiple ways, more than I can explain. I am appreciative to work alongside this extraordinary professor and glad to have him as a mentor.

I would also like to thank the school of Aerospace and Mechanical Engineering. I would especially like to thank Dr. Harold Stalford and Dr. Wilson Merchan.
Both of these professors are genuine people and they have contributed to my success more than they will ever know.

Finally, I would like to thank my parents and family members for their endless support throughout this entire process. I have learned a great deal from everybody and will continue to grow in every facet of my life. I cannot thank everybody enough.

## Table of Contents

Acknowledgements ..... iv

Table of Contents ..... v

List of Tables ..... vii

List of Figures ..... viii

Abstract ..... xii

Chapter 1: Introduction ..... 1

1.1 Introduction to Shale Resources ..... 1

1.2 Phase Behavior ..... 8

1.3 Research Goal ..... 13

1.4 Scope of Thesis ..... 13

Chapter 2: Predicting Fluid Density In Nanopores Using The Cylindrical Form Of the Simplified Local Density Model Coupled With the Peng Robinson Equation Of State ..... 15

2.1 Background and Previous Work ..... 15

2.1 Model Description ..... 21

2.1.1 SLD-PR EOS Multicomponent Cylindrical Model ..... 21

2.1.2 Pore Size Distribution Model ..... 32

2.1.3 Shale Gas in Place Calculations ..... 35

2.1.4 Manipulating Pore Size Distributions with the Gamma Probability Density Function ..... 41

Chapter 3: Results and Discussion ..... 46

3.1 Nanoscopic Level ..... 46

3.1.1 Density Distributions under Confinement Effects: Pore Size, Pressure, and Temperature Sensitivities ..... 46
3.2 Molecular Level ..... 52
3.2.1 Component Compositional Distributions ..... 52
3.3 Macroscopic Level: Multicomponent Shale Gas in Place Calculations with Adsorbed-Phase Considerations ..... 62
3.3.1 Langmuir Monolayer Adsorption and SLD-PR EOS Comparisons ..... 62
3.3.2 Pore Size Distribution Sensitivity Study ..... 68
Chapter 4: Conclusions ..... 75
References ..... 77

## List of Tables


3.1 Bulk Composition of Four Component Mixture ..... 47

3.2 Compares the Average Adsorbed Phase Density Across a 10 nm Pore with the Bulk Density Value Evaluated at a Pressure of 3000 psia and Temperature of 300°F ..... 53

3.3 Multicomponent Mixture Composition and Thermodynamic Properties ..... 63

3.4 Langmuir and SLD-PR EOS Calculation Parameters ..... 63

3.5 Gamma Distribution and Statistical Parameters ..... 68

## List of Figures


1.1 Current and prospective shale gas and shale oil plays in North America as of May 2011 (EIA 2011) ..... 2

1.2 EIA outlook of natural gas production by source for the United States from 2013-2040 (EIA 2015) ..... 3

1.3 North America tight oil production from January 2005-Febuary 2014 (EIA 2014) ..... 4

1.4 Profit margin of different types of reserve replacement (Ozkan 2014a) ..... 5

1.5 Comparison of FIB-SEM (left) and HIM (right) images of a Bossier shale sample (Cananaugh and Wallis 2015). ..... 7

1.6 Compares the production decline of vertical wells in conventional plays (red) and horizontal wells in unconventional plays (blue) (Ozkan 2014b) ..... 8

2.1 Pore size distribution from a MICP test of a Barnett gas shale core (Bruner and Smosna 2011) ..... 18

2.2 Magnified image of a kerogen sample with cylindrical pores of various sizes.. 23

2.3 Cylindrical model showing that the fluid-solid interactions are a function of the pore size (R) and distance from the center of the cylindrical geometry (r) ..... 25

2.4 Flow chart for SLD-PR EOS multicomponent model algorithm ..... 30

2.5 Pore size distribution of Barnett gas shale. The pore throat radius distribution ranges between 1.8 nm to 2,100 nm ..... 33

2.6 Flow chart to determine average density of a pore size distribution starting with incremental mercury injection data ..... 34

2.7 Conceptual model for gas storage in organic rich shale ..... 37

2.8 Illustrates the differences in calculation procedure between the Langmuir method and the SLD-PR EOS method ..... 40

2.9 Graphs of various gamma distributions with different values of k and θ..... 42

2.10 Graph of a gamma probability density function. The area under the curve is equal to one..... 43

2.11 Schematic showing the graphical interpretation of the area under the curve of a gamma probability density function. The difference between the area between two values of r represents the pore volume radius contribution for a given radius $r_i$ ..... 44

3.1 Density profiles of a multicomponent gas mixture consisting of 4 components across a five and ten nm cylindrical pore at a temperature of 300 °F ..... 48

3.2 Compares the average adsorbed phase density value across a 5 and 10 nm cylindrical pore to the bulk density values across a wide range of pressures at a fixed temperature of 300 °F..... 49

3.3 Density profiles across a range of temperatures at a pressure of 3000 psia for a 5 nm pore..... 51

3.4 Fluid density distribution of a multicomponent mixture consisting of 40% methane, 30% ethane, 20% propane, and 10% butane for a 10 nm cylindrical pore at a pressure of 3000 psia and temperature of 300°F ..... 53

3.5 Compositional distributions across a 10 nm pore for a four component mixture containing methane, ethane, propane, and butane at a pressure of 3000 psia and temperature of 300°F..... 54

3.6 Compares the compositional distribution of methane within the 10 nm pore under confinement effects to the bulk phase composition ..... 55
3.7 Compares the compositional distribution of ethane within the 10 nm pore under confinement effects to the bulk phase composition ..... 56
3.8 Compares the compositional distribution of propane within the 10 nm pore under confinement effects to the bulk phase composition ..... 57
3.9 Compares the compositional distribution of butane within the 10 nm pore under confinement effects to the bulk phase composition ..... 58
3.10 Compositional distributions across a 10 nm pore for a five component mixture containing methane, ethane, propane, butane, and pentane at a pressure of 3000 psia and temperature of 300°F..... 60
3.11 Compositional distributions across a 10 nm pore for a six component mixture containing methane, ethane, propane, butane, pentane, and hexane at a pressure of 3000 psia and temperature of 300°F ..... 61
3.12 Total gas storage capacity calculated values using the two separate calculation procedures for multicomponent mixtures..... 64
3.13 Adsorbed gas storage capacity calculated values using the two separate methods for a multi-component mixture..... 65
3.14 Adsorbed gas volume percentage difference based on the values calculated in Figure 3.13..... 66
3.15 Free gas storage capacity calculated values using the two separate methods for a multi-component mixture ..... 67
3.16 Pore volume distribution for Case 1 ..... 69

3.17 Pore volume distribution for Case 2 ..... 69

3.18 Pore volume distribution for Case 3 ..... 70

3.19 Pore volume distribution for Case 4 ..... 70

3.20 OGIP values for Cases 1-4 across a wide pressure range ..... 71

3.21 Average pore size distribution densities for Cases 1 through 4 and bulk density values across a wide range of pressures ..... 73

## Abstract

The pores in shale gas reservoirs are represented on a nanometer scale. In addition to having smaller pore sizes than conventional reservoirs, shale gas reservoirs exhibit different mechanisms of gas storage, i.e. gas stored as adsorbed gas. In a confined environment the physics of fluid transport do not conform to Darcy flow. Current and ongoing research efforts have documented that more appropriate physical models are needed to describe flow in nanopourous media. In particular, predicting the density of fluid within a shale environment becomes a critical factor to model flow. Density is a basic transport property that influences the rate at which momentum, heat, and matter is transferred. Understanding density is important because it influences basic fluid transport. Making more accurate density predictions inside nanopores is imperative to predict transport more precisely. Further, density is instrumental in determining the gas storage capacity, transport of fluids, reserve estimation, and long term production forecasting and planning of shale reservoirs.

Prediction of density in shale formations is a complicated issue and the simplified density model (SLD) coupled with an equation of state has provided considerable insight into how density changes in a nanoscale environment. Our approach applies the cylindrical form of the SLD-Peng Robinson EOS model to study the effects of confinement on density in a shale gas formation. In particular, our study provides meaningful insight of gas behavior on a nanoscopic, molecular, and macroscopic level. At the nanoscopic level we examined the density distribution of a multicomponent mixture and observed its dependence on properties such as pressure, temperature, and

pore size. At the molecular level we studied the interactions between the fluid molecules and porous wall inside nanopores by analyzing compositional distributions of multicomponent gas mixtures within the pore space. Currently, compositional distributions cannot be routinely observed or measured by laboratory experiments due to physical constraints. At the macroscopic level, we examined the significance of pore size distributions on density by considering identical pore volumes with the aid of the gamma probability density function.

The conclusions derived from this work are as follows:

- Density in shale formations is influenced by pore size due to the fluid-wall interactions and the resulting Van der Waal forces.
- The presence of micropores in shales is associated with more gas in place when pore volumes are identical because the density in smaller pores is larger.
- In a confined environment, the adsorbed phase density is influenced by pore size, temperature, and pressure.
- The overall size of an organic molecule has a significant effect on its adsorption potential. Larger molecules have a tendency to occupy the majority of the pore space along the pore wall.
- Pore size distribution has a tremendous impact on average density in a shale formation and neglecting pore size distribution was shown to yield more than a 69% error for average absorbed phase density estimates.

# Chapter 1: Introduction

## 1.1 Introduction to Shale Resources

In the last decade, the economic development of ultra-tight formations has become feasible with advancements in technology in the areas of horizontal drilling, completions, and stimulation. Because shale formations have very low permeability, the productivity must be improved by means of hydraulic fracturing and horizontal wells to make production from the reservoir economic. In fact, the permeability of shale formations is so miniscule; Darcy's equation suggests that there should be no flow occurring within the reservoir. For these reasons, the fracture networks produced by hydraulic fracturing (also called the Stimulated Reservoir Volume (SRV)) completely define the drainage volume within shale reservoirs (Mayerhofer et al. 2010). As a result of technological innovations, the U.S has shifted its focus from conventional reservoirs to unconventional reservoirs. Unconventional reservoirs include liquid rich shale, gas shale, tight gas, and coalbed methane. **Figure 1.1** shows the major producing and prospective shale plays in North America as of May 2011.



Source: U.S. Energy Information Administration based on data from various published studies. Canada and Mexico plays from ARI.
Updated: May 9, 2011

**Figure 1.1 — Current and prospective shale gas and shale oil plays in North America as of May 2011 (EIA 2011)**

**Figure 1.2** shows that unconventional gas will play a significant role in the future of the United States energy demand. According to the US Energy Information Administration (EIA), by the year 2040 gas produced from unconventional resources is predicted to contribute to over 50% of the total gas production in the United States (EIA 2013).

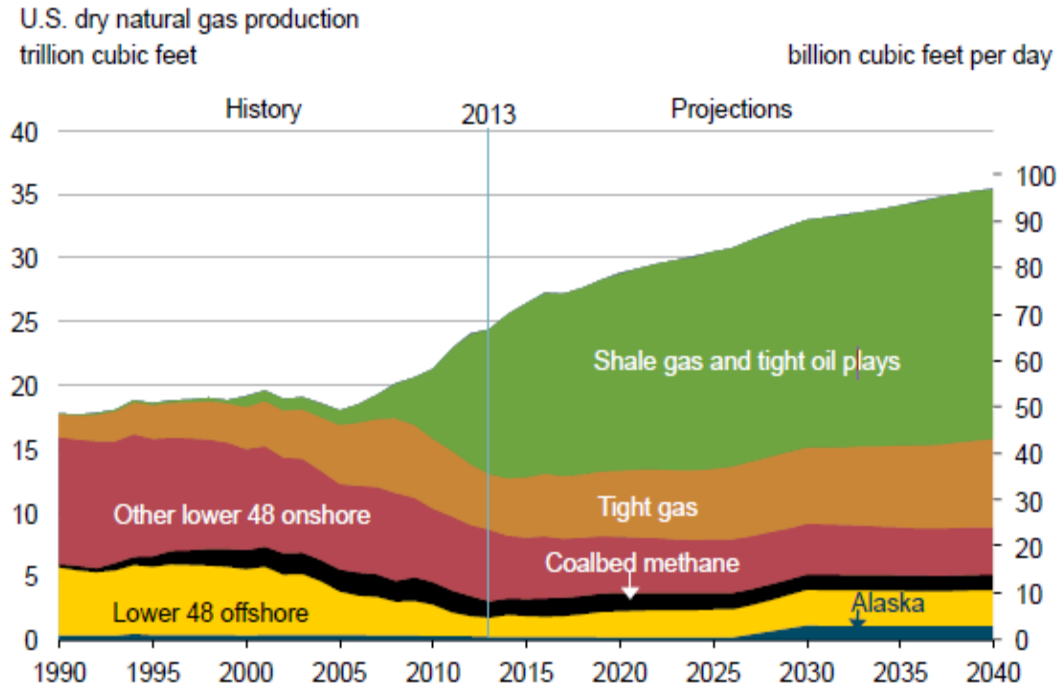


**Figure 1.2 — EIA outlook of natural gas production by source for the United States from 2013-2040 (EIA 2015)**

In addition to increased production from shale gas resources, condensate and liquid oil production from shale oil plays is becoming a larger part of the North America energy mix. **Figure 1.3** shows oil production from North America tight oil plays starting from January 2005.

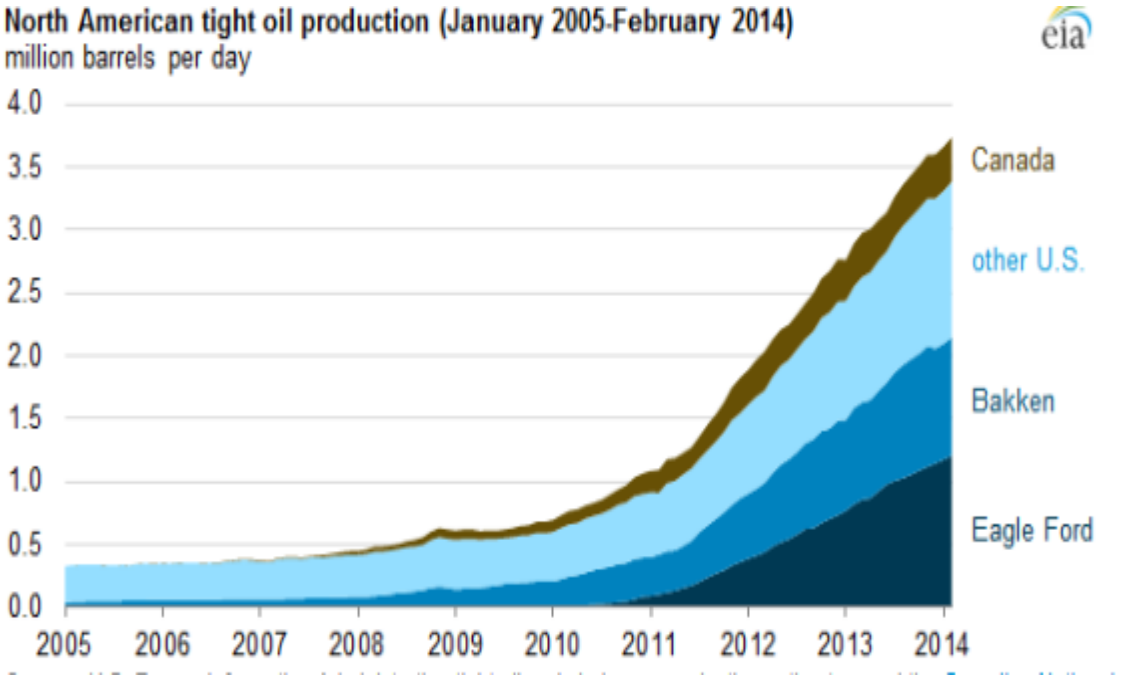


**Figure 1.3 — North America tight oil production from January 2005-Febuary 2014 (EIA 2014)**

Currently, the majority of the tight oil production in North America is produced from the Eagle Ford in South Texas and the Bakken in North Dakota and Montana. In February 2014, oil production in the Eagle Ford was averaging 1.21 MMbbl/d and the Bakken was averaging 0.94 MMbbl/d. During this time period, the two shale plays accounted for 63% of the total tight oil production in North America. The assessment of North America data from the EIA clearly shows that there is an abundance of technically recoverable hydrocarbon from shale resources. These resources have the potential to impact both the political and economic landscape in the United States for years into the future. Economic forecasts from Ozkan (2014a), demonstrate that the profit margin of unconventionals will eventually succeed those of new conventionals for reserve replacement as shown in **Figure 1.4**.

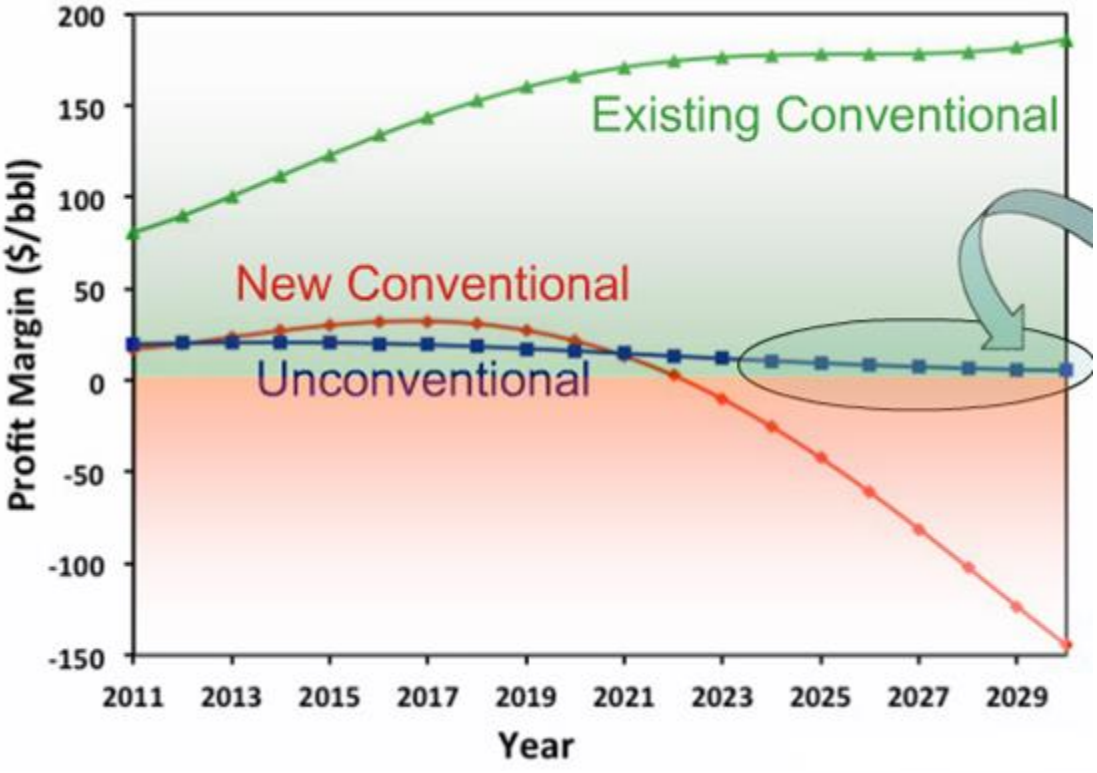


**Figure 1.4 — Profit margin of different types of reserve replacement (Ozkan 2014a)**

From **Figure 1.4** above, it is clear that the largest profit will continue to come from existing conventionals. However as oil and gas companies look to expand their portfolio and replace reserves, new conventionals will eventually prove to be more costly than unconventionals because they will be harder to find and more expensive to produce. To continue to succeed/survive in the oil and gas business, unconventionals will have to be produced and exploited in the near future. Furthermore, new technology will have to be developed to increase the profit margin of production from unconventional resources.

Shale formations are predominantly comprised of consolidated clay particles where the rock serves as both the source rock and reservoir rock for the production of

hydrocarbons (DOE 2009). Recent advancements in high resolution imaging techniques have allowed the microstructure of shale samples to be investigated. For example, scanning electron microscopy (SEM) coupled with focused ion beam (FIB) techniques can produce 3D and 2D images of shale samples (Curtis et al. 2011, Driskill et al. 2013). Using these two techniques together has provided key insight into the petrophysical properties of shale formations, including pore size distribution, porosity, connectivity, and TOC content (Zhang et al. 2012). Improved imaging technology continues to enhance our understanding of shale formations. The most recent advancement in imaging technology, Helium Ion imaging (HIM), includes much greater detail. Compared to SEM and FIB imaging techniques, HIM is able to show sharper pore boundaries and provides a higher resolution of pores less than 10 nm in diameter (Cananaugh and Wallis 2015). **Figure 1.5** shows images of a shale sample using FIB-SEM and HIM imaging techniques.

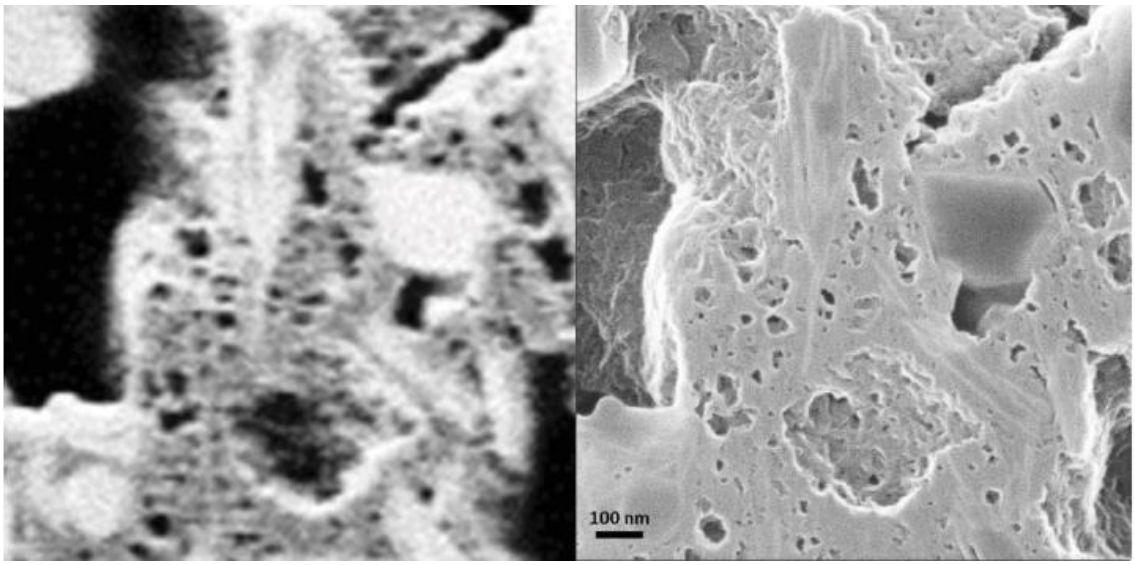


**Figure 1.5 — Comparison of FIB-SEM (left) and HIM (right) images of a Bossier shale sample (Cananaugh and Wallis 2015).**

The images distinguish organic matter (kerogen) from clay and other minerals. Additionally it reveals the amount of void space and the size and distribution of nanopores within the sample. In shale formations, the introduction of confinement effects and kerogen alters the phase behavior of the fluid within the nanopores, causing the fluid to be adsorbed along the pore walls. The fluid-wall interactions cause the fluid to deviate significantly from its bulk state properties thus altering fluid critical properties, density, compressibility factor, viscosity, orientation profiles, structural properties of chemical compounds, and other fluid properties (Jin, Ma, and Jamili 2013). As a consequence of confinement effects, current mathematical models used by industry cannot accurately describe the storage and transport of hydrocarbons in shale reservoirs. In order to carry out meaningful reservoir engineering of shale formations, one needs to understand the phase behavior of the fluid within organic rich nanopores.

## 1.2 Phase Behavior

Although the production of shale plays in the US has increased significantly in the past decade, hydrocarbon flow in nanoporous media is not fully understood. The low permeability (1 to .0001 md) of shale formations and high initial production rates followed by a high decline rate makes it difficult to predict performance and EURs for unconventional reservoirs (Xu et al. 2015). **Figure 1.6** compares the production decline curves of a conventional and unconventional well.

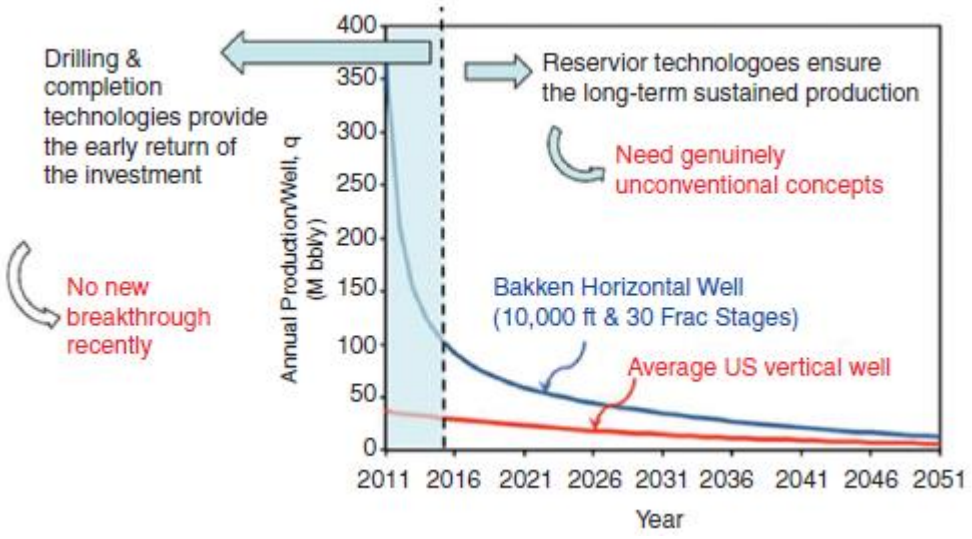


**Figure 1.6 — Compares the production decline of vertical wells in conventional plays (red) and horizontal wells in unconventional plays (blue) (Ozkan 2014b)**

Specifically, fluids in shale plays exhibit significantly different flow properties and phase behavior. This is a result of confinement effects and fluid-wall interactions. Understanding the migration and phase behavior of hydrocarbons in nanopores is critical for continued growth and sustainability of unconventional hydrocarbon resources. Traditional phase behavior models, requiring a cubic equation of state (EOS),

are inadequate for describing fluid behavior in shale formations. Current engineering practice is to apply traditional phase behavior models with minor adjustments to fulfill industry immediate needs, however they have limited capabilities. To develop a more fundamental understanding of flow in nanoporous unconventional reservoirs, researchers have been conducting experimental and numerical studies on hydrocarbon phase behavior in shale formations in hopes of delivering better tools to practicing engineers.

Numerous studies have demonstrated that fluid systems in nanopourous media exhibit different properties and behavior from those observed in the bulk state. There have been a large number of experimental studies related to the physical adsorption of hydrocarbons on solid surfaces. Such studies are especially important to the transportation and storage of hydrocarbons in unconventional reservoirs. In an exhaustive review, Menon (1968) summarized adsorption behavior of fluids under high pressure for various nanoporous media. Experimental results revealed adsorption isotherms at sufficiently high pressures always exhibited a maximum followed by a decrease in adsorption capacity with increasing pressure. Menon's study was limited to single component gases. Sigmund et al. (1973) experimentally and theoretically investigated the effect of curvature and pore size on the phase behavior of hydrocarbon binary mixtures. He found that for pore sizes less than 10 nm, bubble point pressures decreased and vapor compositions where significantly altered from measurements taken in a conventional PVT cell. Experimental data in Zarragoicoechea and Kuz (2004) revealed that critical properties of single component gases in confined porous media

was suppressed compared to its bulk state. Zeigermann et al. (2009) investigated diffusion properties of n-pentane in mesopores undergoing a phase transition to the supercritical state and found similar results. Comparing phase behavior measurements of n-pentane in three different pore sizes, a decrease in pore critical points was observed with decreasing pore size across a wide range of temperatures. Wang et al. (2014) applied nanofluidic devices to visualize phase behavior of pure and multicomponent hydrocarbon mixtures under nanoconfinment. They used two parallel micro-channels that were connected perpendicular to 21 nano-channels to simulate a connected pore distribution system. After reducing the pressure drop incrementally, they discovered that vaporization first occurred in the large pores. As a result, the composition and the bubble point pressures of the remaining liquid in the channels were constantly changing throughout the pressure depletion process. All of the experiments described above suggest the phase behavior of fluids is altered in small pores. However, conclusions derived from these experiments vary and a common consensus has not been achieved. The disagreement of lab data is most likely due to measurements taking place in a nanoscale environment, which proves to be a difficult task with current lab instruments.

Prediction of phase behavior in nanopores is a difficult issue and poses an enormous challenge for conventional laboratory experiments. To circumvent the problem of experimental measurements, thermodynamic numerical models have been used. Some of the most frequently applied numerical models include molecular dynamics simulation, grand canonical statistical ensemble, density functional theory, and modified equations of state. Ambrose et al. (2012) used molecular dynamic simulation

to investigate the adsorption of methane in small, carbon slit pores at various temperatures to predict a density profile. The methane density profiles showed that the density values were significantly greater near the pore walls, exceeding twice the value of the bulk phase density in some instances. In addition, they observed that as pore size decreased, adsorbed phase density increased. Using Monte Carlo simulation methods, Hartman et al. (2011) numerically predicted the adsorbed phase density of methane in a graphite slit pore. Their results suggested that the amount adsorbed was sensitive to pore size and inversely related to temperature. Devegowda et al. (2012) applied modifications to existing numerical simulation software to analyze the phase behavior of a gas condensate fluid in shale gas reservoirs. They recorded the liquid dropout percentage in nanopores of 2, 4, and 5 nm of a gas condensate sample by applying a modified EOS. There results showed that pore proximity had beneficial effects of reducing liquid dropout. They generalized that it is likely that condensate dropout may never occur in smaller pores, thus enhancing well productivity in unconventional systems. The variation of critical properties in porous media characterized by pore size distributions was also investigated with numerical approaches. Using Monte Carlo simulation, Ortiz, López-Álvarez, and López (2005) considered the capillary condensation effect of methane in a uniformly sized pore system and pore size distribution of nanotubes. A decrease in critical temperature values was observed in both systems with decreasing pore size. However compared to a uniformly sized porous system, fluid-tube interactions dominated fluid-fluid interactions in a random distribution of nanopores, hence the adsorption of vapor and liquid phases increased. Because shale reservoirs are characterized by pore size distributions on the nanometer

scale, consideration must be given to fluid-fluid and fluid-solid interactions in such systems in order to accurately model the phase behavior of hydrocarbon fluids. Michel Villazon et al. (2011) developed a model to describe the transportation of gas in shale reservoirs taking into account real gas behavior and effects of pore size distributions. Their study indicated that two effective pore sizes are required to characterize gas flow in shale reservoirs, i.e. a correction factor related to absolute permeability and a transport correction. Numerical simulation of phase behavior in shale resources provides insight into the storage and transport properties of hydrocarbon fluids at the atomic level. Most notably, it provides a time lapsed evolution of a dynamic system, which otherwise might be difficult or impossible to realize by laboratory experiments. More details on the application and implication of various numerical models in regards to shale gas research will be discussed in later chapters.

In conclusion, the transport and storage of hydrocarbon fluids in unconventional shale resources is not fully understood. The presence of nanopores and organic matter in shale reservoirs has altered the phase behavior of fluids and cannot be accurately described by traditional PVT measurements. Experimental results from laboratory measurements have revealed that TOC content, size and surface area of the pores, and geological conditions have an impact on the mechanisms of storage and transport of fluids in shale reservoirs (Clarkson and Bustin 1999, Ross and Marc Bustin 2009). However due to lab instrument and measurement constraints, the data has been sporadic and inconsistent in regards to engineering applications. Another approach to investigating the phase behavior of fluids in nanopores is with numerical simulation. Numerical simulation

approaches are able to reveal more detailed adsorption and diffusion phenomena within nanopores at the atomic level. In addition numerical approaches can bypass constraints presented to current lab measuring and reporting techniques.

## 1.3 Research Goal

The goal of our research is to investigate the effects of confinement on hydrocarbon phase behavior. In this thesis, we have proposed to use the cylindrical form of the simplified local density model coupled with the Peng-Robinson equation of state to solve the hydrocarbon local density distribution for a multicomponent gas mixture within a given pore size. We used the mathematical model to study the interactions between the fluid molecules and porous wall inside the nanopores by analyzing compositional distributions of multicomponent gas mixtures. Additionally, sensitivity analysis was performed to study the effects of temperature, pressure, and pore size on the density distribution of a multicomponent gas mixture. Further, we extended this model to study the effects of pore size distribution on gas storage in shale formations by developing a calculation procedure that includes core data, fluid characterization, pressure, and temperature. Sensitivity analysis was performed with the aid of the gamma distribution to see the effects of pore size distribution on Original Gas in Place values when pore volumes are identical.

## 1.4 Scope of Thesis

This thesis contains four chapters. Chapter 1 provides an updated assessment of data on shale resources, a literature review of the challenges of shale research, and research goal

and motivation as pertaining to this thesis. Chapter 2 outlines the mathematical model described by Simplified Local Density Theory and provides the methodology for Original Gas in Place Calculations of pore size distributions using MICP data coupled with the cylindrical SLD-PR EOS algorithm. Chapter 3 provides the results from our analysis which includes case studies and sensitivity analysis. Chapter 4 includes conclusions derived from our work.

# Chapter 2: Predicting Fluid Density In Nanopores Using The Cylindrical Form Of the Simplified Local Density Model Coupled With the Peng Robinson Equation Of State

## 2.1 Background and Previous Work

There are many types of models that are used for describing adsorption of fluids under high pressure. These models range from empirical fits, such as multilayer adsorption Brunauer-Emmet-Teller (BET) theory (Lowell and Shields 1991) and the Langmuir model (Langmuir 1918), to computational intensive thermodynamic based methods such as Density Functional Theory (DFT) (Ma and Jamili 2014b), Molecular dynamics (Alder and Wainwright 1959), Grand Canonical Monte Carlo Simulation (GCMCS) (Al Ismail and Horne 2014, Van Megen and Snook 1982), and Ideal Adsorption Solution Theory (IAST) (Myers and Prausnitz 1965). The Langmuir model assumes that the absorbed substance on a surface does not exceed one molecule in thickness. In addition the Langmuir model is based on experimental results taken at low pressures which allow for easier measurement of adsorbed gases (Langmuir 1918). Recent studies have shown that the Langmuir monolayer adsorption model is inadequate in modeling adsorption, especially at high pressures (Dhanapal et al. 2014). BET theory extends the Langmuir model to multilayer adsorption phenomena, however the assumptions that goes into the model limits its application in quantifying storage in shale reservoirs. The BET and Langmuir models assume that there are no lateral adsorbent interactions between molecules. In addition, both empirical methods are limited to subcritical temperatures and assumes ideal gas behavior in the vapor phase (Rangarajan, Lira, and

Subramanian 1995). Although these empirical models are computationally undemanding, their scope of application is limited and unable to quantify storage in organic shale nanopores. Theoretically sound methods such as Molecular Dynamic Simulations (MDS) numerically solve Newton's equations of motion both in equilibrium and non-equilibrium statistical mechanics (Alder and Wainwright 1959). In a Grand Canonical Monte Carlo scheme, a Markov chain of molecular configurations is produced by performing three trial moves: (1) particle displacement, (2) particle insertion, and (3) particle removal (Frenkel and Smit 2001). The random insertion and deletion of particles continues until a solution is achieved. However, such methods require a significant amount of computing time and/or a supercomputer to model adsorption in nanopores, which makes MDS and GCMCS too computationally demanding for engineering practical use. Ideal Adsorption Solution Theory describes adsorption behavior with Raoult's law for vapor-liquid equilibrium. The disadvantage of IAST is it is only valid for ideal solutions. Thus the model is unable to correctly model adsorption isotherms for non-ideal systems frequently encountered in engineering practice (Erto, Lancia, and Musmarra 2011). The Simplified Density Model (SLD) predicts the adsorption behavior of hydrocarbons by utilizing a cubic equation of state (EOS). The SLD model reduces mathematical complexity and has broad applications because of its EOS foundation. Contrary to Langmuir and BET models, the SLD model includes interactions between the adsorbed molecules and the pore walls. In addition, it is orders of magnitude faster than molecular dynamic and Grand Canonical Monte Carlo Simulations (GCMC). The purpose of the SLD model is to bridge the gap between the computationally intensive but analytically sound simulation models and the

limited but widely used empirical methods (Rangarajan, Lira, and Subramanian 1995).

In past studies the SLD-Peng-Robinson Equation of State (SLD-PREOS) model has been extended to different pore geometries, pure component, and multicomponent mixtures. Fitzgerald et al. (2003) applied the SLD procedure to model adsorption and predict recovery of pure methane in coalbeds assuming a slit geometry. Peng and Yu (2008) confirmed that adsorption and desorption isotherms from DFT agreed extremely well with GCMC simulations for argon and nitrogen pure component gases when modeled in a cylindrical pore geometry. Most prior studies have focused on the effect of nanoconfinement on a single pore size. However, in reality pore sizes rarely exist as a uniform pore size in reservoirs. Instead pores form complex interconnected networks that communicate with each other, affecting the gas storage and transport of hydrocarbons. **Figure 2.1** shows the pore size distribution of a Barnett shale core sample from a mercury injection capillary pressure test.

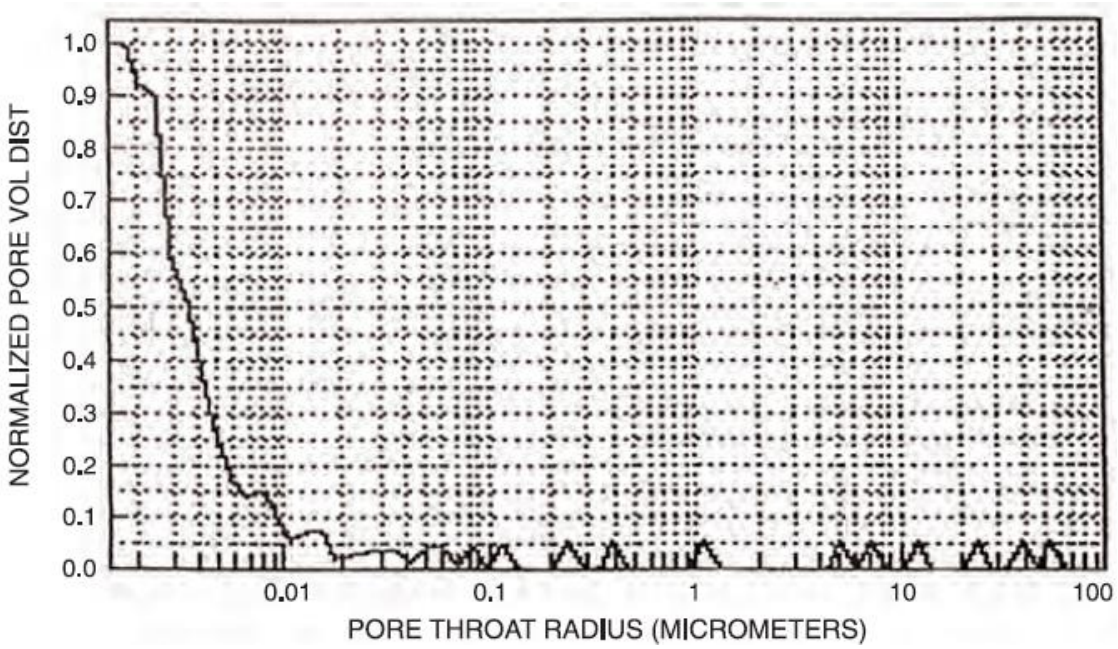


**Figure 2.1 — Pore size distribution from a MICP test of a Barnett gas shale core (Bruner and Smosna 2011)**

The results from **Figure 2.1** confirm 80% of the pore throats have a radius of less than 5 nm, with pore throat sizes as small as 1 nm and possibly smaller (Bowker 2007). Similarly, mercury injection profiles for both crushed and plugged core samples from the Eagle Ford liquid rich shale reservoir demonstrated that the dominant pore size fell below 10 nm for the majority of the samples tested by Honarpour et al. (2012). FIB-SEM 3D reconstruction of Utica shale samples revealed that the pore size distributions was dominated by submicron pores with the highest frequency of pores corresponding to 20 nm in diameter (Zhang et al. 2012). Typically pore sizes for organic rich shale reservoir rocks range from a few nanometers to hundreds of nanometers with the majority of the pore volume contribution coming from pore sizes less than 10 nm (Rezaee 2015). The effect of pore size distributions has rarely been studied and remains

a challenging subject for researchers. For instance, Dhanapal et al. (2014) attempted to extend the PR-EOS to determine the effective pore size for shale pore size distributions. However, several case studies have shown that it is extremely challenging to define an effective pore size for a given pore size distribution. Wang et al. (2014) investigated the effect of pore size distribution on the phase behavior of hydrocarbon mixtures by combining the Peng Robinson-EOS with capillary pressure. However the authors noted that there model was only valid for pores that are greater than 10 nm in diameter. In general, a fundamental approach for describing the effect of pore size distributions of shale reservoirs on gas storage modeling has not been reached.

It is well recognized that the interactions between the fluid molecules and the porous walls inside nanopores alters the phase behavior of fluids. Overwhelming experimental evidences suggests that the fluid density, critical properties, and other thermo-physical properties significantly deviate from their bulk values when confined to nanopores. Often experimental results are in disagreement with each other. Trebin and Zadora (1968) reported that the dew point of gas condensate mixtures can be 10 to 15 percent higher than those observed in a traditional PVT cell. Using nano-fluidic chips to simulate porous tubes, Parsa, Yin, and Ozkan (2015) observed that the gas phase condensed to a liquid phase at pressures below the standard vapor pressure. Using controlled pore glasses (CPGs) , Luo, Lutkenhaus, and Nasrabadi (2015) observed that the bubble point is dramatically effected by pore size with deviations as great as ±15 K in bubble point temperature, suggesting two populations of evaporating fluid. Sigmund et al. (1973) reported that bubble point pressures decrease at higher surface curvatures

inside porous media. The reason shale systems are difficult to describe is because gas shale reservoirs are typically organic rich. This implies that an appreciable amount of hydrocarbons can be adsorbed/stored inside nanopores due to the strong surface-fluid interactions. These interactions lead to a heterogeneous distribution of molecules within the pore space in which conventional bulk phase thermodynamics fail to describe. In these cases, an accurate description of multicomponent gas adsorption is required to accurately estimate reserves, rates, and gas in place. Further, a better understanding of how the fluid behaves on a molecular level is crucial to understanding mechanisms of mass, momentum, and energy transport in confined environments. Many studies have been dedicated to describing competitive adsorption of multicomponent mixtures. Lyklema (2005) and Lipatov, Todosijchuk, and Chornaya (1993) developed models describing competitive adsorption of liquid media. Appelo, Hendriks, and van Veldhuizen (1993) performed multicomponent adsorption experiments of metal ions to model transport in aquifers and soils. Fewer studies have investigated multicomponent distributions inside graphite nanopores. Applying the SLD-PR model, Ma and Jamili (2014a) were able to predict the compositional distribution of a binary mixture across a 10 nm carbon slit. At this time, there is no explicit description of how a fluid exceeding two components interacts in a confined environment on a molecular level. We seek to address this issue in this study.

In this work, the cylindrical form of the SLD-Peng-Robinson Equation of State (SLD-PR EOS) model will be used to investigate the effects of confinement on density in a shale gas formation. As a first step towards a better understanding of adsorption

behavior in organic rich shale, this study specifically focuses on the following:

- Describing the influence of pore size, temperature, and pressure on the fluid density distribution of a multicomponent mixture by applying sensitivity analysis with the SLD-PR EOS model.
- Providing an explicit understanding of competitive adsorption by analyzing compositional distributions of a multicomponent gas mixture using the SLD-PR EOS model.
- Adopting the SLD-PR EOS model to quantify the pore distribution effect on estimation of original gas in place (OGIP) for a multi-component gas shale reservoir.

In addition, we will compare original gas in place estimates between a newly proposed procedure using the SLD-PR EOS model and the most widely used model in the industry, the Langmuir monolayer adsorption model. Further, the effect of pore size distribution on OGIP calculations will be evaluated with the aid of the Gamma distribution.

## 2.1 Model Description

### *2.1.1 SLD-PR EOS Multicomponent Cylindrical Model*

Multiple studies have confirmed that the SLD model has been capable of describing the adsorption and desorption of gases for coalbed sequestration of $CO_2$ and coalbed methane production (Chen et al. 1997, Fitzgerald et al. 2003). The same thermodynamic and equilibrium relations used in previous studies will be extended to fluid mixtures to

predict the density distribution in cylindrical shaped pores that represent kerogen nanopores inside shale formations.

The SLD model makes the following basic assumptions (Chen 2005):

- The chemical potential at any point near the adsorbent surface is equal to the chemical potential of the bulk phase.
- The chemical potential at any point above the surface is the sum of the fluid-fluid and fluid-solid interactions.
- The attractive potential between fluid and solid is independent of the number of molecules at and around a point.

The SLD-Peng Robinson framework is based on the principles of chemical equilibrium and is outlined in the following. Instead of using the slit shaped pore space model, which is reasonable for coalbed methane reservoirs, we propose to use the cylindrical shaped model for the pore space in the organic matter. As shown in **Figure 2.2** below by Curtis, Ambrose, and Sondergeld (2010), kerogen pores are better characterized by a cylindrical shaped pore space rather than a slit shaped pore space.

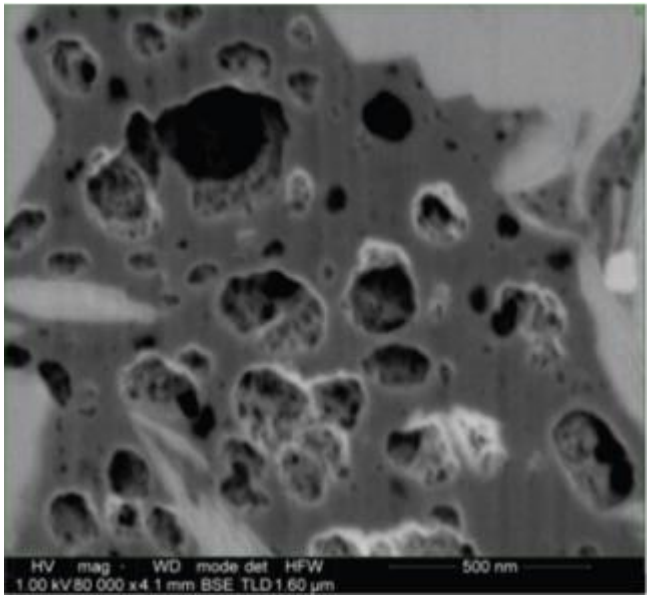


**Figure 2.2 — Magnified image of a kerogen sample with cylindrical pores of various sizes**

Let r represent the radial distance from the center of a cylindrical pore. The chemical potential of a fluid within a cylindrical porous system at a given radial distance $r_i$ is a function of the fluid-fluid and fluid-solid interaction potentials. Hence, when the system is at equilibrium the chemical potential (μ) at any location ($r_i$) from the center of a cylindrical pore can be expressed by the following equation:

$$\mu(r) = \mu_{Bulk} = \mu_{ff}(r_i) + \mu_{fs}(r_i) \quad (1)$$

The subscripts "Bulk", "ff", and "fs" refers to the bulk fluid, fluid-fluid, and fluid-solid interactions, respectively. At equilibrium, the chemical potential is constant throughout the pore, i.e. there is no chemical potential gradient from the outer wall of the pore structure to the bulk fluid in the center of the pore. The chemical potential of a non-ideal bulk fluid expressed in terms of fugacity is the following:

$$\mu_{\mathrm{Bulk}} = \mu_0(T) + RTln\left(\frac{f_{Bulk}}{f_0}\right) \quad (2)$$

The subscript "0" denotes the reference state. Similarly, the fluid-fluid chemical potential is defined in the equation below:

$$\mu_{\mathrm{ff}}(\mathrm{r}) = \mu_0(\mathrm{T}) + \mathrm{RTln}(\frac{\mathrm{f_{ff}(r)}}{\mathrm{f_0}}) \quad (3)$$

For a cylindrical geometry, the fluid-solid chemical potential expressed in its reduced form can be written as the following:

$$\mu_{\mathrm{fs}} = \mathrm{N_A}\psi(\mathrm{r},\mathrm{R}) \quad (4)$$

Where $N_A$ is Avogadro's number and $\psi$ is the fluid-solid potential. Note that the fluid-solid potential is a function of the pore radius (R) and radial distance from the center of the pore (r). It is well documented that under confinement effects a fluids thermodynamic properties are altered and deviate from their bulk values (Travalloni et al. 2010, Zarragoicoechea and Kuz 2004). Thus to describe the molecular interactions (molecule-molecule and molecule-wall effects), Lennard-Jones Potential was applied. Many previous studies assume a slit model, i.e. an open system to model the interaction between the adsorbent and adsorbed hydrocarbon (Chen et al. 1997, Fitzgerald et al. 2003). Our study modified upon the SLD slit model framework of previous authors by assuming that the adsorbed molecules reside in a cylindrical pore structure, i.e. a closed system, as shown in **Figure 2.3**.

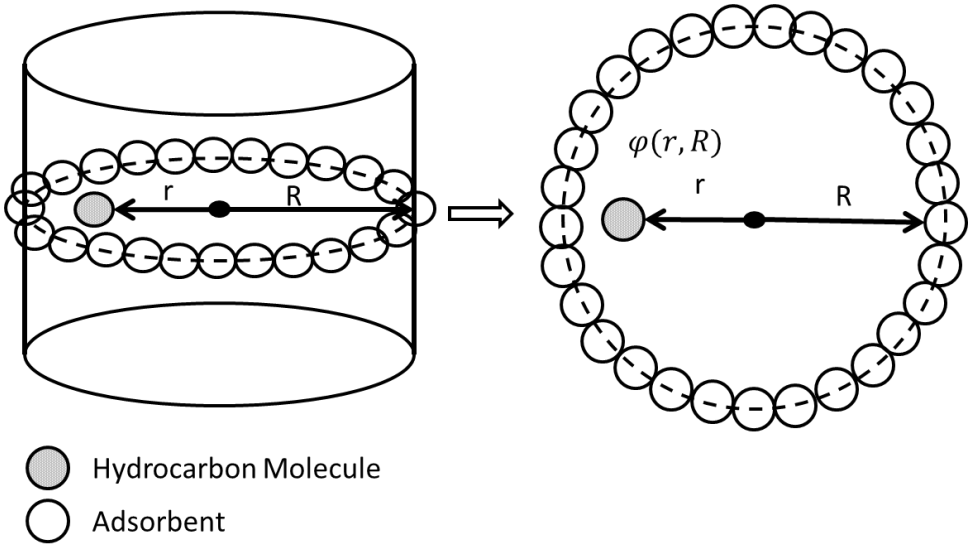


**Figure 2.3 — Cylindrical model showing that the fluid-solid interactions are a function of the pore size (R) and distance from the center of the cylindrical geometry (r)**

Tjatjopoulos et al. (1988) was the first to develop a mathematical model to describe fluid-solid interactions for a cylindrical surface. Unlike the slit model, a cylindrical surface includes the effects of curvature. A more detailed comparison between the slit pore model and the cylindrical pore model along with the major assumptions that go into either is discussed in Saito and Foley (1991). The fluid-solid potential across a cylindrical pore space can be modeled by the Leonard-Jones (6-12) potential function given below:

$$\psi(\mathrm{r},\mathrm{R}) = \pi^2 \rho_{\mathrm{atoms}} \varepsilon_{\mathrm{fs}} \sigma_{\mathrm{fs}}^2 \left[ \frac{63}{62} \left[ \frac{\mathrm{r}}{\sigma_{\mathrm{fs}}} \left( 2 - \frac{\mathrm{r}}{\mathrm{R}} \right) \right]^{-10} \mathrm{F}\left[ -\frac{9}{2}, -\frac{9}{2}; 1; \left( 1 - \frac{\mathrm{r}}{\mathrm{R}} \right)^2 \right] \right.$$
$$\left. - 3 \left[ \frac{\mathrm{r}}{\sigma_{\mathrm{fs}}} \left( 2 - \frac{\mathrm{r}}{\mathrm{R}} \right) \right]^{-4} \mathrm{F}\left[ -\frac{3}{2}, -\frac{3}{2}; 1; \left( 1 - \frac{\mathrm{r}}{\mathrm{R}} \right)^2 \right] \right] \tag{5}$$

The equation above is defined in the work of Ravikovitch, Haller, and Neimark (1998) where $\rho_{atoms}$ is the number of carbon plane atoms per unit area, $\epsilon_{fs}$ is the

fluid-solid interaction energy parameter, $\sigma_{fs}$ is the fluid-solid average molecular diameter, R is the radius of the cylindrical pore, and F is the hypergeometric series function. $\rho_{atoms}$ is taken to be a value of 38.2 atoms/nm$^2$. The fluid-solid parameter is defined as the following:

$$\sigma_{fs} = \frac{\sigma_{ff} + \sigma_{SS}}{2} \tag{6}$$

In our analysis the solid-solid molecular diameter ($\sigma_{ss}$) is taken to be the value of graphite, i.e. 0.335 nm (Chen 2005). Substituting **Eq. (2)** through **(4)** into **Eq. (1)**, the fluid-fluid fugacity can be solved in terms of the Lennard-Jones (6-12) Potential function and the bulk fugacity as shown in the equation below:

$$f_{ff}(r) = f_{bulk} \exp\left(-\frac{\psi_{fs}(r)}{RT}\right) \tag{7}$$

In this analysis, the bulk fugacity and bulk density is determined with the PR-EOS. The PR-EOS fundamental formula is shown below:

$$\frac{P}{\rho RT} = \frac{1}{1-\rho b} - \frac{\alpha_T \rho}{RT\left[1+\left(1-\sqrt{2}\right)\rho b\right]\left[1+\left(1+\sqrt{2}\right)\rho b\right]} \tag{8}$$

where $\alpha_T$ and b are given by the mixing rules (McCain 1990):

$$b = \sum y_j b_j \tag{9}$$

$$a_T = \sum\sum y_i y_j \left(a_{Ti} a_{Tj}\right)^{\frac{1}{2}} \left(1-\delta_{ij}\right) \tag{10}$$

$$b_i = 0.07780 \frac{RT_c}{P_c} \tag{11}$$

$$a_{T_i} = 0.45724 \alpha_j \left(\frac{R^2 T_c^2}{P_c}\right) \tag{12}$$

$$B_j' = \frac{b_j}{b} \tag{13}$$

$$A_j' = \frac{1}{a_T} 2a_{Tj}^{\frac{1}{2}} \sum_i y_i a_{Ti}^{\frac{1}{2}} (1 - \delta_{ij}) \tag{14}$$

The subscripts "i" and "j" represent different components of a mixture. The PR-EOS **Eq. (8)** can be expressed in terms of the Z-factor as shown below:

$$z^3 - (1 - B)z^2 + (A - 2B - 3B^2)z - (AB - B^2 - B^3) = 0 \tag{15}$$

$$A = \frac{\alpha_T P}{R^2 T^2} \tag{16}$$

$$B = \frac{\mathrm{bp}}{\mathrm{RT}} \tag{17}$$

The cubic form of the PR-EOS has three roots. The lowest root is the z factor of the liquid ($Z_L$), the middle root is discarded, and the highest root is the z factor of the vapor phase ($Z_v$) (Whiston and Brule 2000). In our analysis, the z factor of the gaseous state was applied, i.e. the largest root value. Subsequently, the bulk phase density and bulk fugacity can be determined with the following equations from the PR-EOS:

$$\rho_{bulk} = \frac{\mathrm{P}}{\mathrm{TRZ}} \tag{18}$$

$$\ln\left(\frac{f_i^{Bulk}}{P}\right) = -\ln(z - B) + (z - 1)B_j' - \frac{A}{2^{1.5}B}\left(A_j' - B_j'\right) \ln\left(\frac{z + \left(2^{\frac{1}{2}} + 1\right)B}{z + \left(2^{\frac{1}{2}} + 1\right)B}\right) \tag{19}$$

The fluid-fluid fugacity for a component can then be determined by substituting the bulk fugacity solved from **Eq. (19)** into **Eq. (7).** The fluid-fluid fugacity can be expressed in terms of the local density ($\rho(r_i)$) for component i as shown in the equation below:

$$\ln\left(\frac{f_i^{ff}}{y_i P}\right) = \frac{b_i}{b}\left(\frac{P}{RT\rho(r_i)} - 1\right) - \ln\left[\frac{P}{RT\rho(f_i)} - \frac{Pb}{RT}\right] + \frac{a_{ff}(z)}{2\sqrt{2}bRT}\left(\frac{b_i}{b} - \frac{2\sum_j y_j a_{ij}^{ff}(z)}{a_{ff}(z)}\right)\ln\left[\frac{1+\left(1+\sqrt{2}\right)\rho(r_i)b}{1+\left(1-\sqrt{2}\right)\rho(r_i)b}\right] \quad (20)$$

For the mixture adsorption calculation, half of the diameter of the cylindrical pore is subdivided into a finite number of intervals. The local density at each interval within the cylindrical pore is determined by solving the equilibrium criterion equation **Eq. (1)** subject to the following mole fraction constraint:

$$\sum y_i = 1 \quad (21)$$

For i number of components, there are i+1 unknowns. The unknowns are the mole fraction ($y_i$) for each component and the local density value ($\rho(r_i)$). Consequently, there are i+1 equations needed to solve for the unknowns: An equation of the form of **Eq. (20)** for each component i and the mole fraction constraint **Eq. (21)**. The local density can then be determined by applying a constrained optimization technique to solve the nonlinear system of equations. In our study, the trust regions algorithm was applied. The trust region method combines Cauchy's steepest descent and the Newton Raphson method in a convenient manner to exploit the strengths of both, i.e. it has the convergence speed of the Newton Raphson method when the Hessian matrix is positive definite and is globally convergent like Cauchy's steepest descent method (Ravindran, Ragsdell, and Reklaitis 2006). More details of the numerical optimization technique is discussed in Conn, Gould, and Toint (2000) and its applications to multiphase flash calculations is discussed in Petitfrere and Nichita

(2014). Once the local density profile is developed across the cylindrical pore, the average density can be determined by integration using the equation below:

$$\bar{\rho}_r = \frac{\int_0^R \rho(r)dr}{\int_0^R dr} = \frac{\sum_{i=1}^{N}[\rho(r_i)\,\Delta r_i]}{\sum_{i=1}^{N}[\Delta r_i]} \tag{22}$$

An algorithm to determine the bulk state and adsorbed state densities for a multi-component system using the SLD-PR EOS model is shown in **Figure 2.4** below:

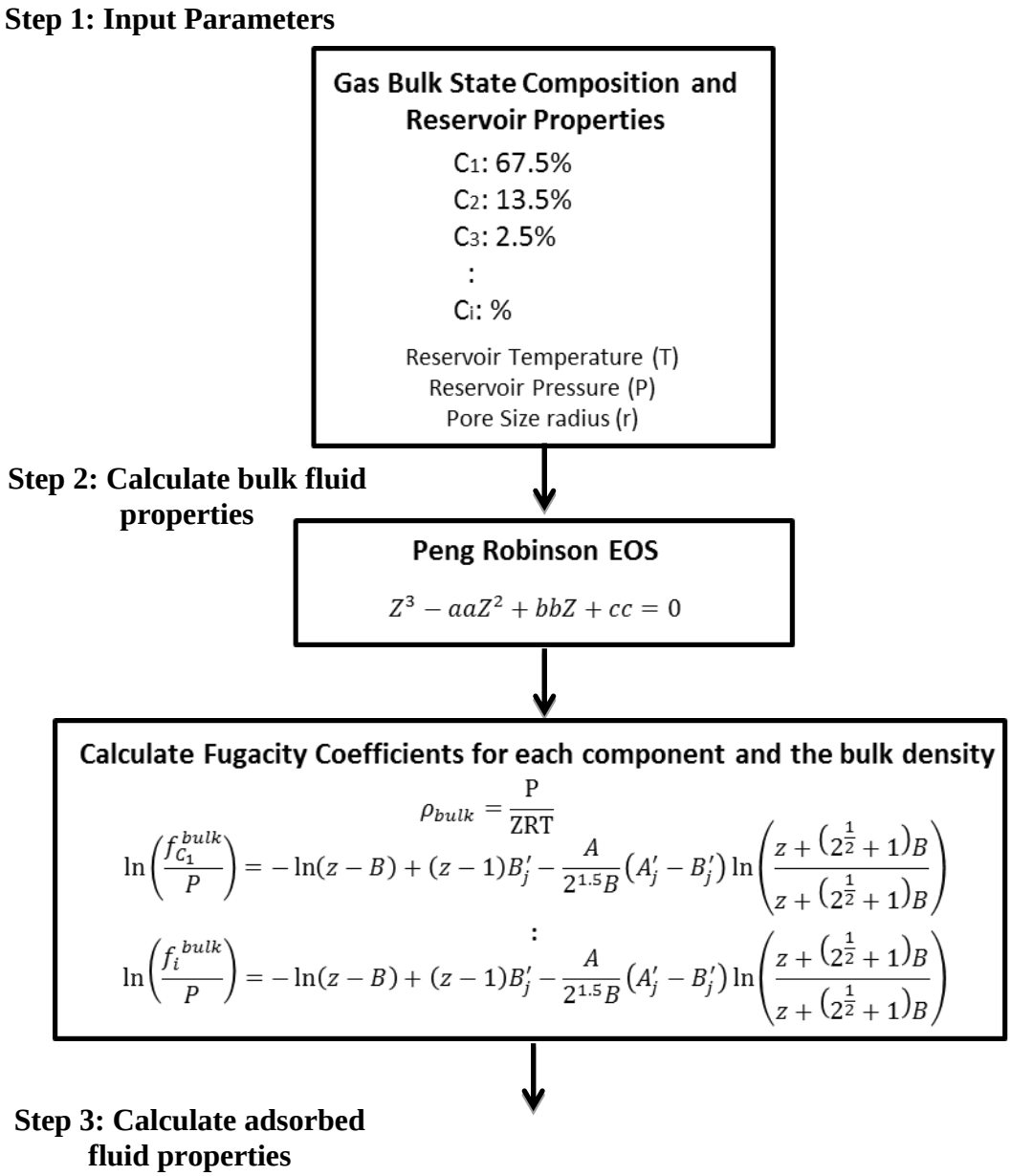

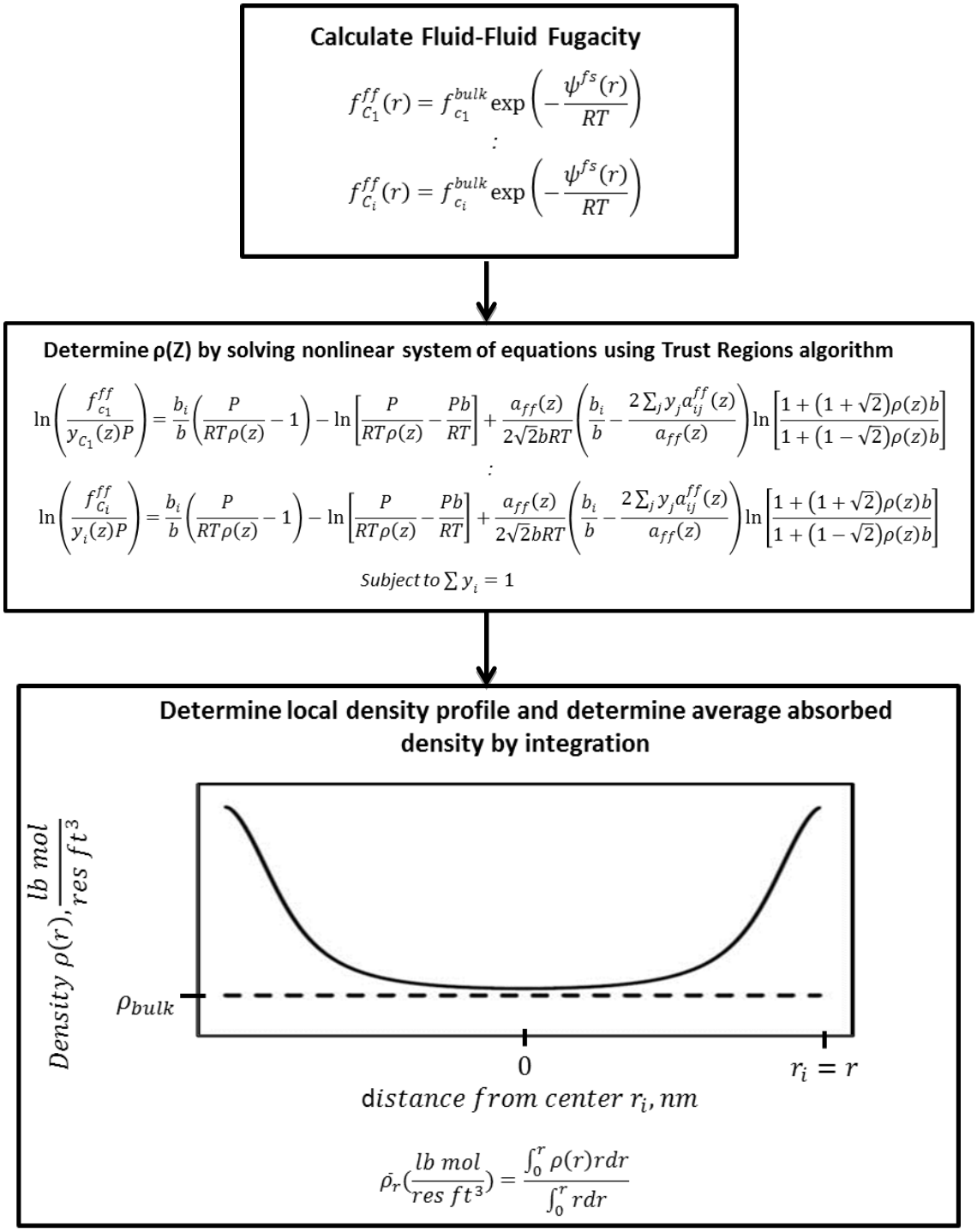


**Figure 2.4 — Flow chart for SLD-PR EOS multicomponent model algorithm**

In summary, the SLD-PR EOS multicomponent algorithm outlined in **Figure 2.4** can be described by the following step by step procedure:

1. The inputs are gas bulk phase characterization, reservoir pressure, reservoir temperature, and pore size.
2. Calculate phase Z factors from the PR-EOS and select the largest root which represents the Z factor for the vapor phase.
3. Calculate component bulk fugacity's ($f_i^{bulk}$) from the PR-EOS and the bulk density of the multicomponent mixture **Eq. (18)**.
4. Calculate component fluid-solid potential at a position $r_i$ **Eq. (5)**.
5. Calculate the fluid-fluid fugacity for each component($f_i^{ff}$).
6. Calculate local density $\rho(r_i)$ by solving the constrained nonlinear optimization problem using the trust regions algorithm.
7. Repeat calculation procedure described in steps 1-6 until the local density profile is determined across the cylinder.
8. Calculate the average adsorbed phase density $\bar{\rho}_r$ by integration **Eq. (26)**.

Note that the bulk phase and adsorbed phase densities are expressed in units of lb-mol/ft$^3$. A conversion constant of 379.4 $\frac{scf}{lb-mol}$ will be valuable in the proceeding sections for determining the original gas in place for organic rich shale from the calculated density values.

*2.1.2 Pore Size Distribution Model*

Shale pore size distributions can be characterized by a variety of measuring techniques, e.g. Nuclear Magnetic Resonance (NMR), Mercury Injection Capillary Pressure (MICP) tests, or by FIB-SEM imaging (Sondergeld et al. 2010). An advantage of MICP tests is they can be performed on fresh cuttings as well as cores. In addition, MICP tests allow the gathering of porosity data and pore size distributions. A MICP test is performed by placing a rock sample in an empty instrument chamber then flooding it with mercury. Pressure is incrementally increased in the chamber, forcing the mercury to fill the pore throats of the sample. The experiment is carried out to 60,000 psi allowing the mercury to intrude into the smallest of pore throats. The volume of mercury that has intruded the rock by the end of the experiment is the volume of the porosity accessed in the sample. Fig. 1 in Sondergeld et al. (2010) shows an incremental mercury intrusion ($V_{in}$) curve as a function of mercury injection pressure ($P_c$) for a Barnett gas shale. Mercury injection pressure can be converted to a pore throat radius by applying Young's equation given below:

$$r = \frac{2\sigma cos\theta}{P_c} \tag{23}$$

Using Young's equation with a contact angle of 140° and interfacial tension of 480 dyne/cm, the pore size distribution for the Barnett gas shale core sample can be derived. The resulting pore size distribution is shown in **Figure 2.5** below**:**

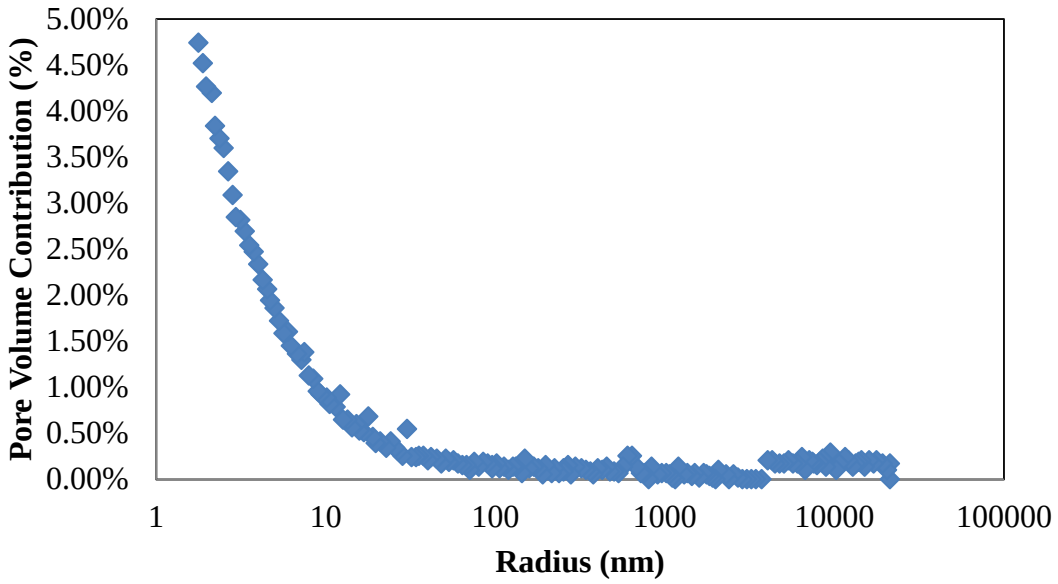


**Figure 2.5 — Pore size distribution of Barnett gas shale. The pore throat radius distribution ranges between 1.8 nm to 2,100 nm**

The flow diagram demonstrates the procedure to derive the average density of a pore size distribution for a gas shale core sample starting with an incremental mercury injection curve from a MICP test:

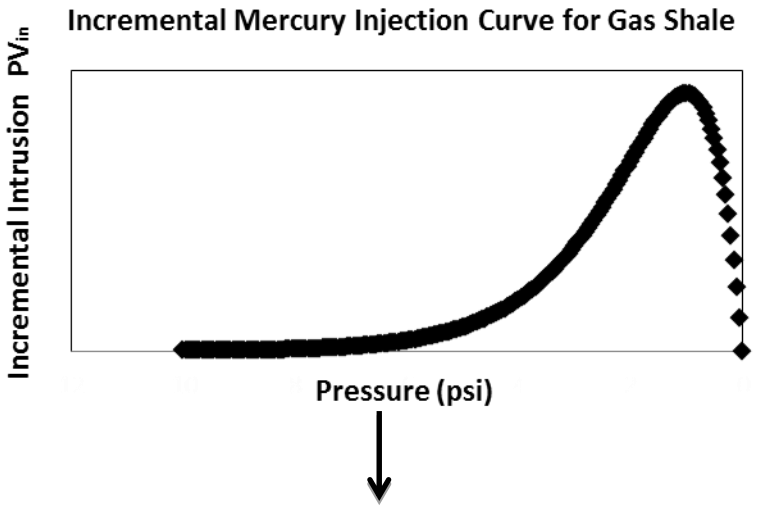

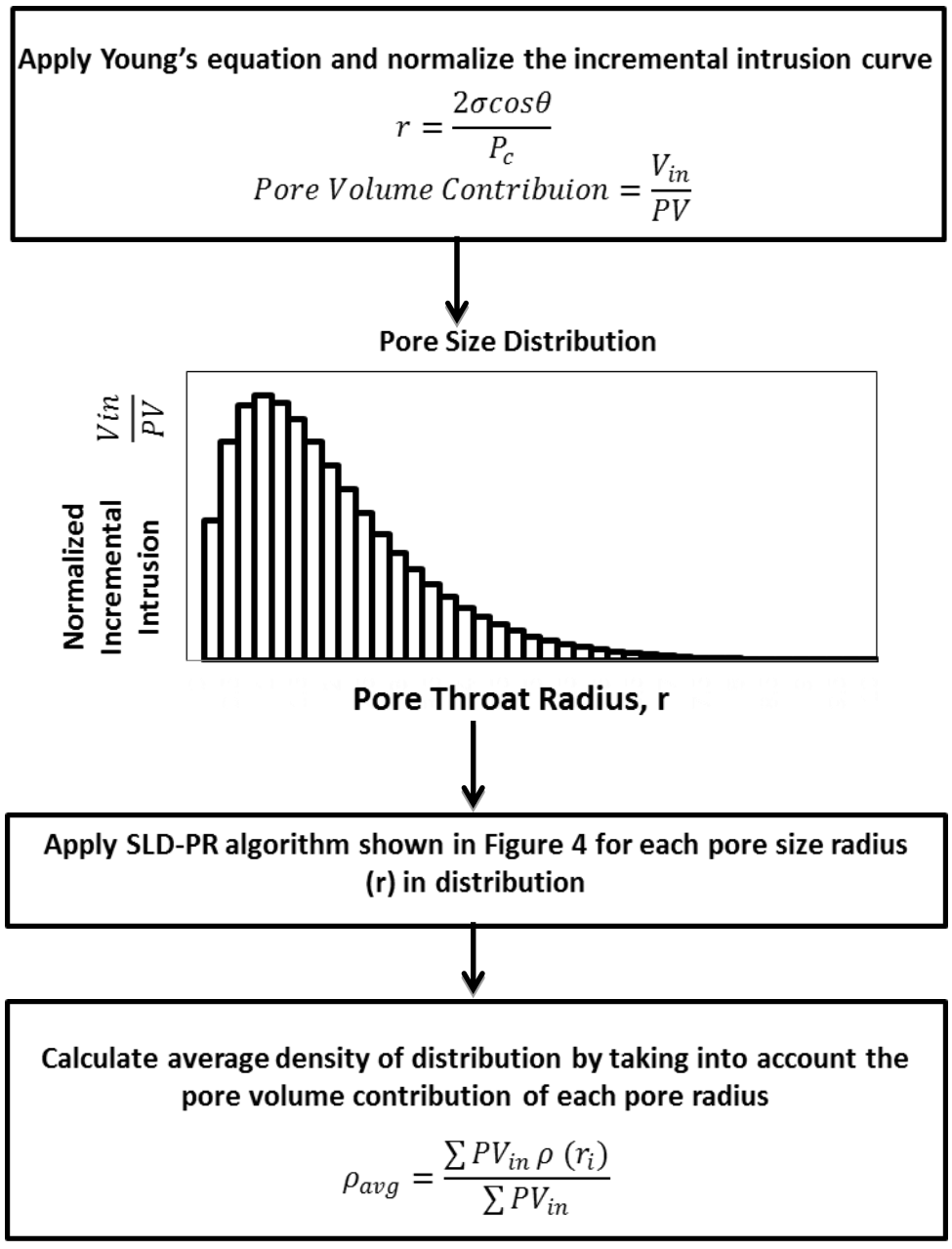


**Figure 2.6 — Flow chart to determine average density of a pore size distribution starting with incremental mercury injection data**

In summary, obtaining the average density of a pore size distribution from a MICP test outlined in **Figure 2.6** can be described by the following step by step procedure:

1. Perform a MICP test on a core sample to obtain the incremental intrusion curve.
2. Convert the pressure to a pore throat radius using Young's **Eq. (23)**. Use the contact angle and interfacial tension for mercury (140°, 480 dynes/cm).
3. Normalize the y-axis of the incremental intrusion curve to get the pore volume contribution of each pore throat size.
4. Plot the pore size distribution.
5. Calculate the average adsorbed density of each pore throat size by applying the SLD-PR EOS algorithm shown in **Figure 2.4**.
6. Calculate the average density of the pore size distribution taking into account the pore volume contribution of each pore throat size.

This procedure will be applied in later examples to calculate OGIP at different pressure values.

### *2.1.3 Shale Gas in Place Calculations*

To accurately predict the gas storage capacity in organic rich shale reservoirs one needs to understand the physical mechanisms for gas trapping. Unlike conventional reservoirs, there are four forms of gas storage in organic rich shale reservoirs. The forms described by Adesida et al. (2011) are the following: **(1)** free gas volume ($G_f$), **(2)** adsorbed gas volume ($G_{ads}$), **(3)** gas dissolved in liquid hydrocarbon ($G_{so}$), and **(4)** gas dissolved in formation water ($G_{sw}$). Hence, the total gas storage in organic rich shale is described by the following equation:

$$G_{st} = G_f + G_{ads} + G_{so} + G_{sw} \tag{24}$$

In standard industry practice, it is assumed that the volume of gas dissolved in formation water and liquid hydrocarbons is negligible for shale gas and coal bed methane reservoirs (Ambrose et al. 2012). However, molecular simulations conducted by Diaz Campos, Akkutlu, and Sigal (2009) suggests gas solubility is enhanced when the fluid system is confined to micropores found in shale reservoirs. Although the work by Diaz Campos, Akkutlu, and Sigal (2009) is insightful, there is no experimental evidence that can validate their model, thus in this paper the gas dissolved in formation water will not be considered. Based on the previous assumptions, **Eq. (24)** reduces to include only the adsorbed gas volume and free gas volume as shown below:

$$G_{st} = G_f + G_{ads} \tag{25}$$

Unlike other rock types, shales contain organic matter in the form of kerogen. The molecular interactions between the organic matter and hydrocarbon molecules allow shales to store a significant amount of gas in an adsorbed state. The free gas resides in the inorganic voids such as macropores, fractures, and fissures (Ambrose et al. 2012). This dual pore system (inorganic/organic) adds additional complexity; however it needs to be accounted for in gas in place calculations. **Figure 2.7** shows a conceptual model of the gas storage mechanisms considered in organic rich shale.

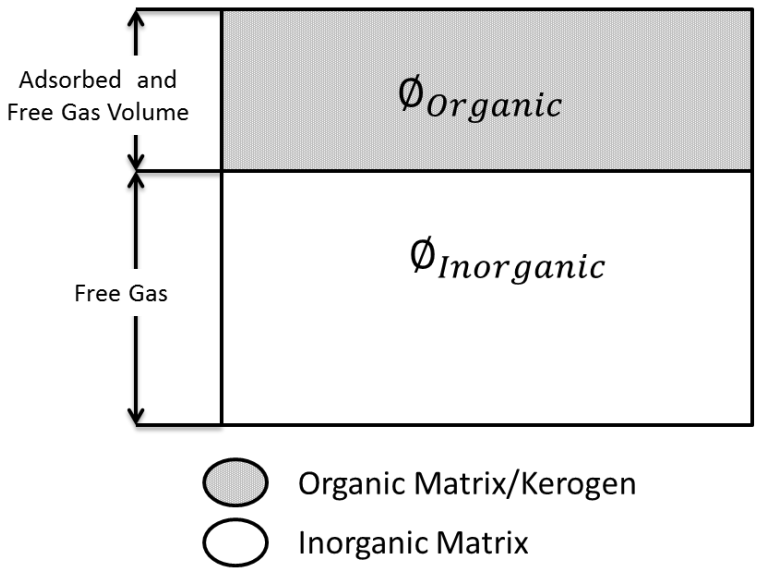


**Figure 2.7 — Conceptual model for gas storage in organic rich shale**

As shown above in **Figure 2.7**, we assume both free and adsorbed gas is associated with the organic pore matrix. This implies that free and adsorbed gas can exist simultaneously within the organic pore space. The contribution of adsorbed and free gas components within the organic pore space is primarily a function of pore size due to fluid-wall effects. Only free gas is found in the inorganic pore space because fluid-wall effects are considered to be negligible. A further discussion on the distribution of organic and inorganic materials in shale and its effect on gas storage can be found in Kang et al. (2011). When a reservoir is depleted to a new pressure, the equilibrium of fluid in both organic and inorganic matter will be re-established in the new condition. Therefore, the produced gas comes from both free gas and adsorbed gas. This conceptual model was used to formulate a procedure to calculate OGIP using the SLD-PR EOS model.

Two procedures of calculating OGIP was evaluated and compared in this work. The methodologies of each calculation are presented below:

**1. Langmuir Monolayer adsorption theory: Free + Adsorbed Gas Calculation:**

In this method, the free gas volume and adsorbed gas volume is considered in OGIP estimations. If we neglect the gas dissolved in water, the governing equations are presented below. Further details on the calculation procedure can be found in Ambrose et al. (2012).

$$OGIP = G_f + G_{ads} \tag{26}$$

$$G_f = \frac{32.0368\varphi_{Total}(1 - Sw)}{\rho_B B_g} \tag{27}$$

$$\varphi_{Total} = \varphi_{organic} + \varphi_{Inorganic} \tag{28}$$

$$G_{ads} = \frac{G_{SL}P}{P + P_L} \tag{29}$$

where: $G_f = free\ gas\ volume\ \left(\frac{scf}{ton}\right)$

$G_{ads} = Adsorbed\ gas\ volume\ \left(\frac{scf}{ton}\right)$

$G_{SL} = The\ Langmuir\ Volume\ \left(\frac{scf}{ton}\right)$

$P_L = The\ Langmuir\ Pressure\ (psi)$

$P = Reservoir\ Pressure\ (psi)$

The Langmuir Volume and Langmuir Pressure are acquired from laboratory measurements of crushed rock samples. The absorbed gas volume value is calculated by an empirical correlation derived from the experimental work of Langmuir (1918) **Eq. (29)**.

**2. SLD-Peng Robinson: Free + Adsorbed Gas Calculation**

Similar to the Langmuir calculation procedure, this method considers the free gas volume and adsorbed gas volume components. However, the SLD-PR EOS algorithm outlined in **Figure 2.4** is used to calculate the average density across the various pore sizes for the organic kerogen pore space. In the inorganic pore space fluid-wall interactions are negligible, thus only a single bulk density value was required to calculate the gas storage contribution from the inorganic pore space. Laboratory measurements are not required for this method. The governing equations are presented below:

$$OGIP = G_f + G_{ads} \tag{26}$$

$$\mathrm{G_f} = \frac{32.0368\varphi_{\mathrm{inorganic}}(1 - \mathrm{Sw})}{\rho_{\mathrm{B}}\mathrm{B_g}} \tag{30}$$

$$G_{ads} = \frac{32.0368\varphi_{organic}(1 - Sw)}{\rho_B B_g} \tag{31}$$

**Figure 2.8** below illustrates the difference in the calculation procedure between the Langmuir method and the new proposed method using the SLD-PR EOS model.

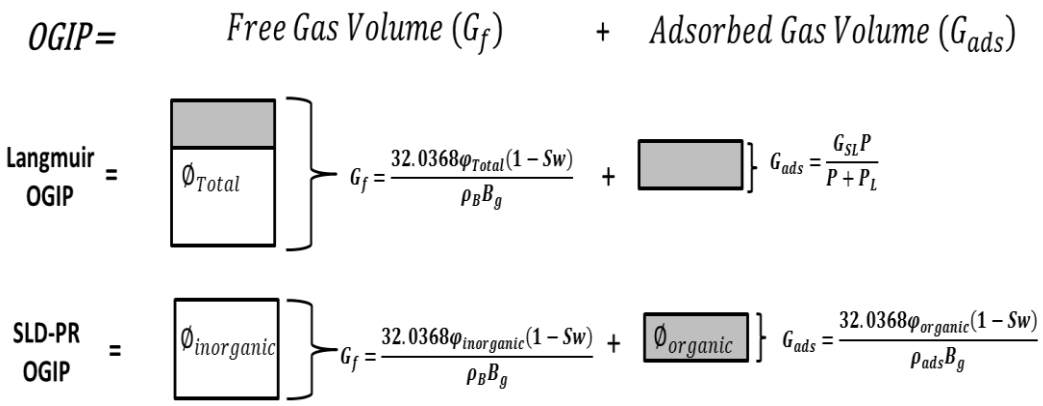


**Figure 2.8 — Illustrates the differences in calculation procedure between the Langmuir method and the SLD-PR EOS method**

As shown above, the Langmuir OGIP calculation procedure associates the free gas volume with the entire pore space likely leading to an overestimation in the amount of total free gas. The adsorbed gas volume is determined by the Langmuir isotherm equation which requires the experimentally determined constants, $G_{SL}$ and $P_L$. Often these constants are inaccurate and sample dependent, producing erroneous results because of the existing limitations on sorption measurement and reporting techniques. More details on data variability of OGIP calculations using the Langmuir isotherm calculation procedure is discussed in Das, Jonk, and Schelble (2012). The new proposed method using the SLD-PR EOS model associates the free gas volume with both the inorganic and organic pore space. However the free gas volume is dependent on the amount adsorbed. Thus the organic pore space may or may not contain free gas. The adsorbed gas volume is only associated with the organic pore space. This agrees with

the conceptual model shown in **Figure 2.7**. In Chapter 3, the OGIP values of the two calculation procedures will be compared.

### *2.1.4 Manipulating Pore Size Distributions with the Gamma Probability Density Function*

Generally, the smaller the pore size the greater the density of the adsorbed phase in the rock due to the fluid-solid interactions. Mosher et al. (2013) compared the densities measured in 0.4 nm and 9 nm sized pores at 1 MPa using molecular simulation. They determined that the 0.4 nm pores contained 84 times more methane than the 9 nm pores. Given the abundance of pore sizes found in shale samples, the consideration of the pore size effect is of utmost importance when carrying out adsorption and reserve studies. As a demonstrative example, this study will consider several samples of identical pore volumes but different pore size distributions to see what effect it has on OGIP values.

For convenience, the gamma distribution will be used to manipulate the pore size distribution for our analysis. The gamma distribution is a continuous probability distribution model with two adjustable parameters: the scale parameter (θ) and the shape parameter (k). Manipulating the value of the scale parameter affects the spread of the distribution. Changing the value of the shape parameter alters the shape of the distribution. The functional form of the probability density function (PDF) for the gamma distribution is the following:

$$f(X;k,\theta) = \frac{1}{\Gamma(k)\theta^k} x^{k-1} e^{-\frac{x}{\theta}} \tag{32}$$

$$\Gamma(k) = \int_0^\infty t^{k-1} e^{-t} dt \tag{33}$$

The mean and variance of the gamma distribution are given by the following equations:

$$\mu_{mean} = k\theta \tag{34}$$

$$\sigma_{std}{}^2 = k\theta^2 \tag{35}$$

The figure below shows the different shapes of the gamma distribution by altering k or θ:

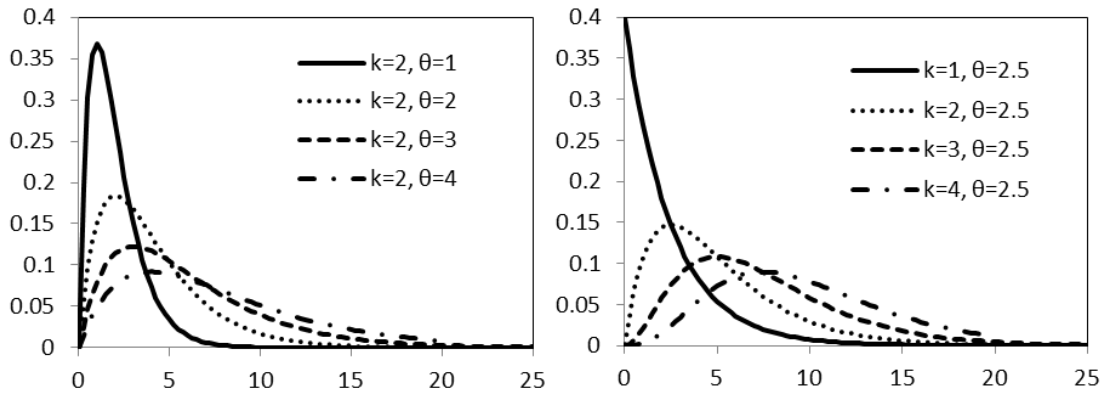


**Figure 2.9 — Graphs of various gamma distributions with different values of k and θ**

As can be seen in the figure above the gamma distribution can take on various shapes and forms. Thus the gamma distribution can model various forms of experimental data (Joshi 2011). In our case, the gamma distribution will allow us to model various pore size distributions while maintaining a constant pore volume.

The continuous gamma distribution probability density function (PDF) is applied to model various pore size distributions by dividing the area under the curve into sections.

By definition, the area under any PDF from 0 to ∞ is equal to one. This is shown schematically in the figure below with the appropriate units for this analysis:

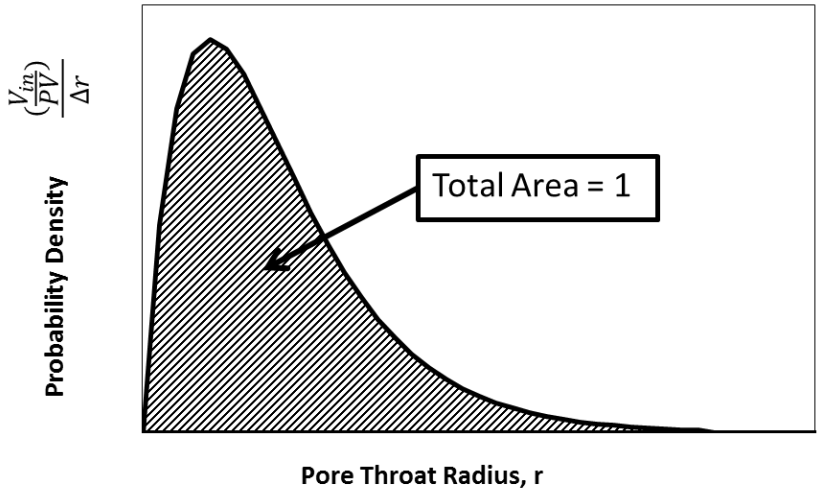


**Figure 2.10 — Graph of a gamma probability density function. The area under the curve is equal to one**

The bin width, $\Delta r$, assures that the area under the curve will always be equal to one. In our analysis, the area of a section is defined as the normalized pore volume fraction $(\frac{V_{in}}{PV})$ for a range of pore throat sizes $r_{i-1}$ to $r_i$. Because the total area under the curve is equal to unity the gamma PDF can be used to model various shapes of a pore size distribution while maintaining a constant pore volume (PV). The pore volume contribution of radius $r_i$ can be determined by the following equation and is schematically illustrated in **Figure 2.11**.

$$\left(\frac{V_{in}}{PV}\right)_{r_i} = \int_{r_i-1}^{r_i} f(x)dr \tag{36}$$

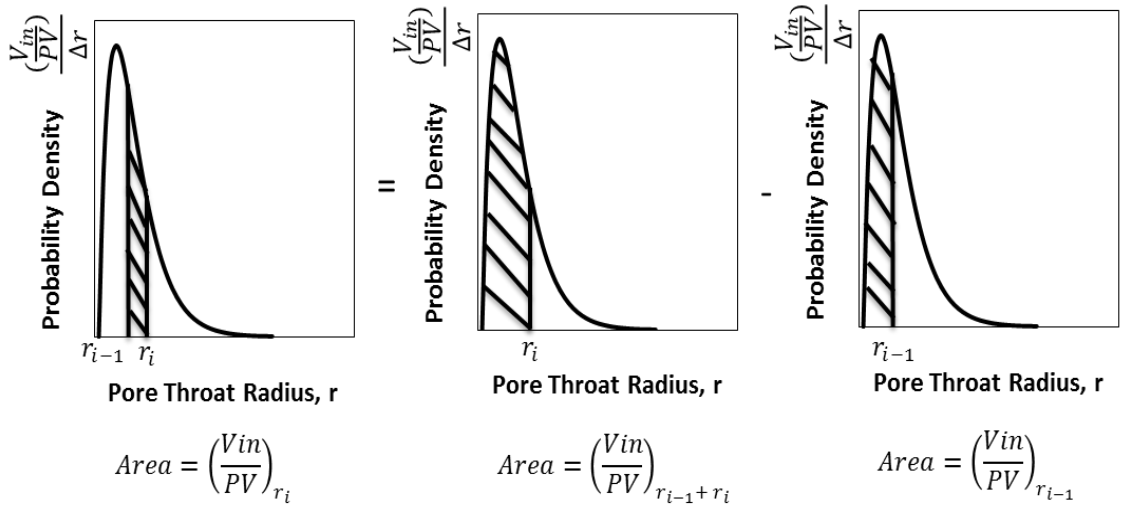


**Figure 2.11 — Schematic showing the graphical interpretation of the area under the curve of a gamma probability density function. The difference between the area between two values of r represents the pore volume radius contribution for a given radius $r_i$**

The above approach can be carried out easily with spreadsheet calculations. Once the pore volume contribution is determined for each pore throat size for a given gamma distribution, the average density of the pore size distribution can be determined using the algorithm in **Figure 2.4**.

In literature, there are many ways to classify small pores in shales, e.g. nanopores, macropores, mesopores. In this work, we will use the International Union of Pure and Applied Chemistry (IUPAC) pore size classification system reported in Sing (1985). The pore sizes are defined below:

- Micropores: Pores with widths less than 2 nanometers

- Mesopores: Pores with widths between 2 and 50 nanometers
- Macropores: Pores with widths greater than 50 nanometers

The IUPAC standard pore classification system is the standard terminology used in the presentation and interpretation of adsorption data. The classification system is even more appropriate for shales because the majority of the shale pore volume consists of nanometer-sized pores.

The presence of extremely small pores in shales is documented in several studies. Schieber et. al (1988) defined shale or mudstone as a fine grained sedimentary rock with a dominant grain size less than 63 μm. Dong et al. (2015) calculated pore size distributions from nitrogen adsorption analysis on representative shale samples. They reported that the dominant pore size fell below 10 nm with the highest frequency of pores contributing being less than 2 nm in diameter (micropores). Rutherford et al. (1997) studied montmorillonite clay with nitrogen and neo-hexane adsorption techniques. They reported the total pore volume of samples contained between 14-66% micropores. In the following sections, the IUAPC pore size classification system will be used to classify pore size distributions.

# Chapter 3: Results and Discussion

The previous chapter was focused on the development of the mathematical model used to study the effects of confinement on phase behavior in nanopores. We discussed the cylindrical form of the SLD-PR EOS model which allows us to predict the fluid density at any location within the pore space. Further, a calculation procedure for average adsorbed phase density considering pore size distributions using MICP data was summarized. In this chapter, we study the effects confinement on the phase behavior of multicomponent mixtures on a nanoscopic, molecular, and macroscopic level. First, we consider the effect of pore size, pressure, and temperature on the density distribution of a multicomponent mixture by performing sensitivity analysis. Second, we study the interactions between the fluid molecules and porous wall inside nanopores on a molecular level by analyzing compositional distributions of multicomponent gas mixtures within the pore space. Lastly, we examine what is happening to the fluid mixture on a macroscopic level by considering the pore size distribution effect on average adsorbed phase density within a core sample using MICP data. We use the calculation procedure in combination with the gamma distribution to compare OGIP estimates of various pore size distributions with identical pore volumes.

## 3.1 Nanoscopic Level

### *3.1.1 Density Distributions under Confinement Effects: Pore Size, Pressure, and Temperature Sensitivities*

In this section, we will investigate the influence of pore size, pressure, and temperature on the fluid density distribution of a multicomponent mixture by applying the

cylindrical version of the SLD-PR EOS model. A four component mixture consisting of methane, ethane, propane, and butane with the following bulk composition shown in **Table 3.1** will be evaluated:

| **Table 3.1 — Bulk Composition of Four Component Mixture** | |
|---|---|
| **Component** | **Bulk Composition Fraction ($z_i$)** |
| $C_1$ | 40% |
| $C_2$ | 30% |
| $C_3$ | 20% |
| $C_4$ | 10% |

It is well recognized that pore size influences the fluid density distributions in a confined space. Consider the multicomponent mixture given in **Table 3.1** in a five and ten nm cylindrical shaped pore. The density distributions across a 5 and 10 nm cylindrical pore are juxtaposed in **Figure 3.1**. The density distributions are evaluated at pressure conditions ranging between 1,000 and 6,000 psia and a temperature of 300 °F.

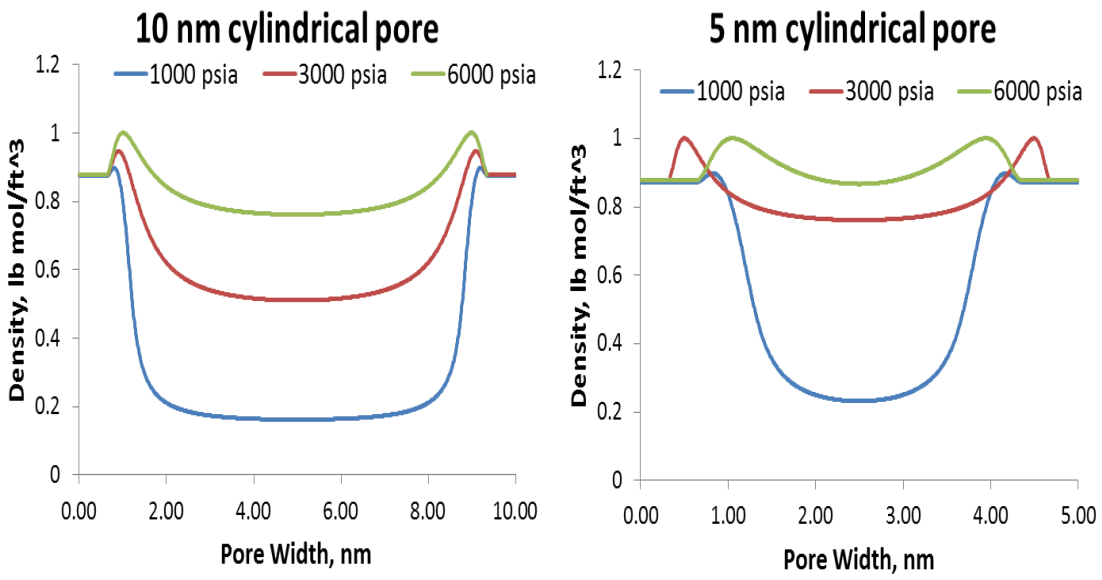


**Figure 3.1 — Density profiles of a multicomponent gas mixture consisting of 4 components across a five and ten nm cylindrical pore at a temperature of 300 °F**

The density profiles from **Figure 3.1** suggest that pore size has a significant influence on the adsorbed phase density of multicomponent gas mixtures. For example, at 3000 psia the average adsorbed phase density in the 5 nm pore (0.82 lb mol/ft^3) is much higher than the average adsorbed phase density of the 10 nm pore (0.65 lb mol/ft^3) at the same pressure. Comparing the density distributions in **Figure 3.1**, it is obvious that the density profile near the center of the pores shifts upwards with decreasing pore size at each pressure. This suggests that the influence of the pore wall becomes more significant as the pore size decreases.

Other than pore size, pressure can influence the density distributions within confined nanopores. As shown in **Figure 3.1** at increasing pressures, the density profiles has a tendency to shift upwards when pore size is fixed. This is expected because as pressure

increases the number of molecules striking the surface per unit time increases, therefore the quantity adsorbed increases. In other words, the number of molecules adsorbed at any moment of time is a function of pressure. At higher pressures, multiple layers of molecules begin to form and most of the adsorption sites along the pore wall are filled. **Figure 3.2** compares the average adsorbed phase density values across a 5 and 10 nm pore to the bulk phase density values over a wide range of pressures for identical fluids.

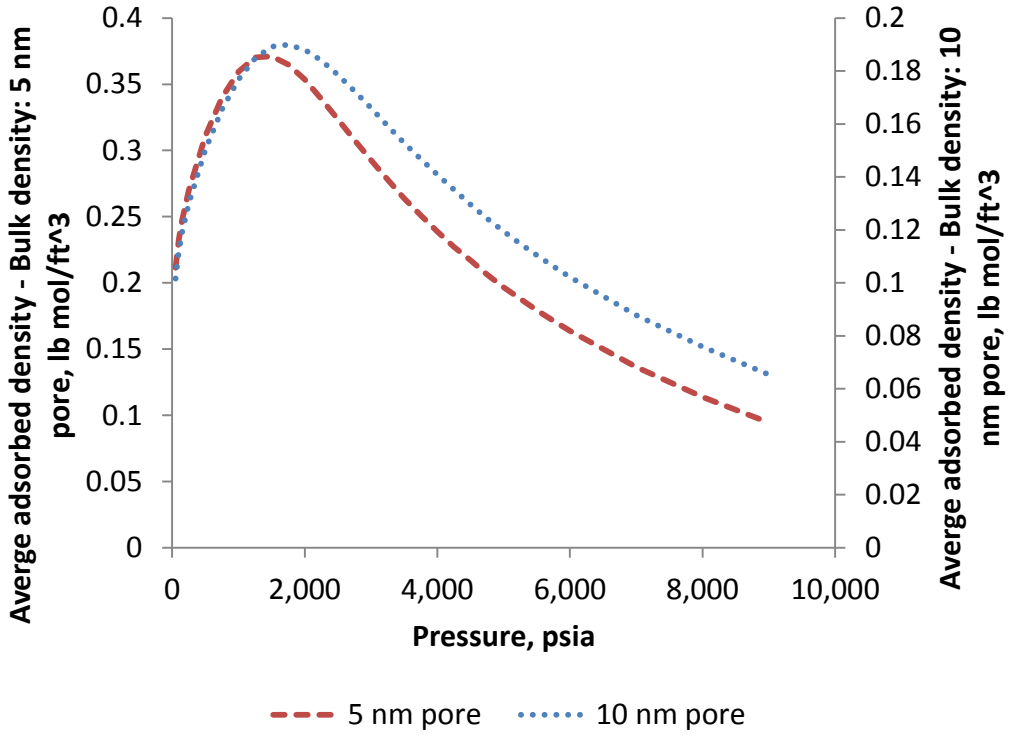


**Figure 3.2 — Compares the average adsorbed phase density value across a 5 and 10 nm cylindrical pore to the bulk density values across a wide range of pressures at a fixed temperature of 300 °F**

At sufficiently high pressures, the difference between the average adsorbed phase density and the bulk density value will show a maximum as indicated in **Figure 3.2**. After this maximum, the average adsorbed phase density begins to approach the bulk density value for both the 5 and 10 nm pore sizes. This suggests that the gas molecules have occupied all the adsorption sites and adsorption no longer occurs. The pressure at which this maximum occurs largely depends on the affinity of the fluid molecules for the surface and pore size. **Figure 3.2** indicates that the 5 nm pore size reaches its maximum adsorbed phase density value at a faster rate than the 10 nm pore size. This is expected because the 5 nm pore size has less surface area or fewer adsorption sites than the 10 nm pore. Further the results imply that pressure has a much greater impact on the amount adsorbed when the fluids are less compressed, i.e. at pressures below the maximum.

Temperature can also influence the density distribution of a multicomponent mixture. The density distribution across a 5 nm cylindrical pore is shown in **Figure 3.3** below across a range of temperatures:

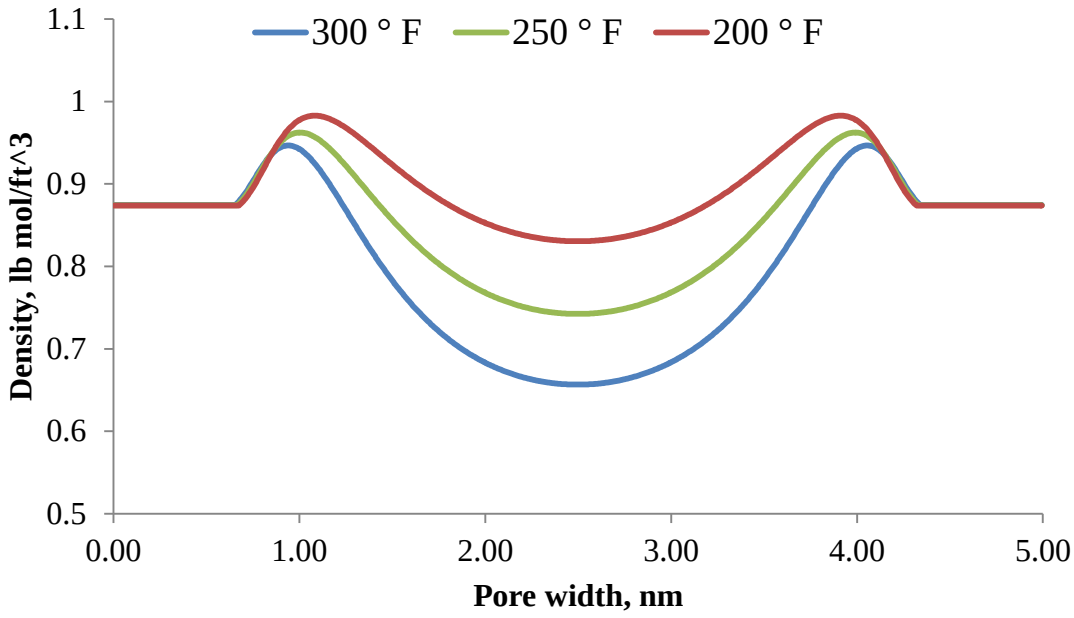


**Figure 3.3 — Density profiles across a range of temperatures at a pressure of 3000 psia for a 5 nm pore**

One observation of interest is the density profile shifts upward with decreasing temperature. This is expected because at lower temperatures, the average kinetic energy of the particles is much less. Because the system has less energy, the adsorption layer involves a much more compact packing. Consequently the density is higher at lower temperatures. The results described above are consistent with the works of Dhanapal et al. (2014) and Hartman et al. (2011). Further, the results are consistent with standard fluid PVT relations, where an increase in temperature results in a decrease in density.

## 3.2 Molecular Level

*3.2.1 Component Compositional Distributions*

In the previous section, the influence of pore size, temperature, and pressure on the fluid density distribution of a multicomponent mixture was investigated. In this section, we will study the effects of confinement on a molecular level by applying the cylindrical form of the SLD-PR EOS algorithm to model the compositional distribution of components within a cylindrical pore. The multicomponent mixture with compositional data given in **Table 3.1** will be investigated.

Consider the multicomponent mixture given in **Table 3.1** with the bulk compositional values. The fluid density distribution of the mixture in a 10 nm pore is given in **Figure 3.4** below. **Table 3.2** compares the average adsorbed density with the bulk density values for this particular case.

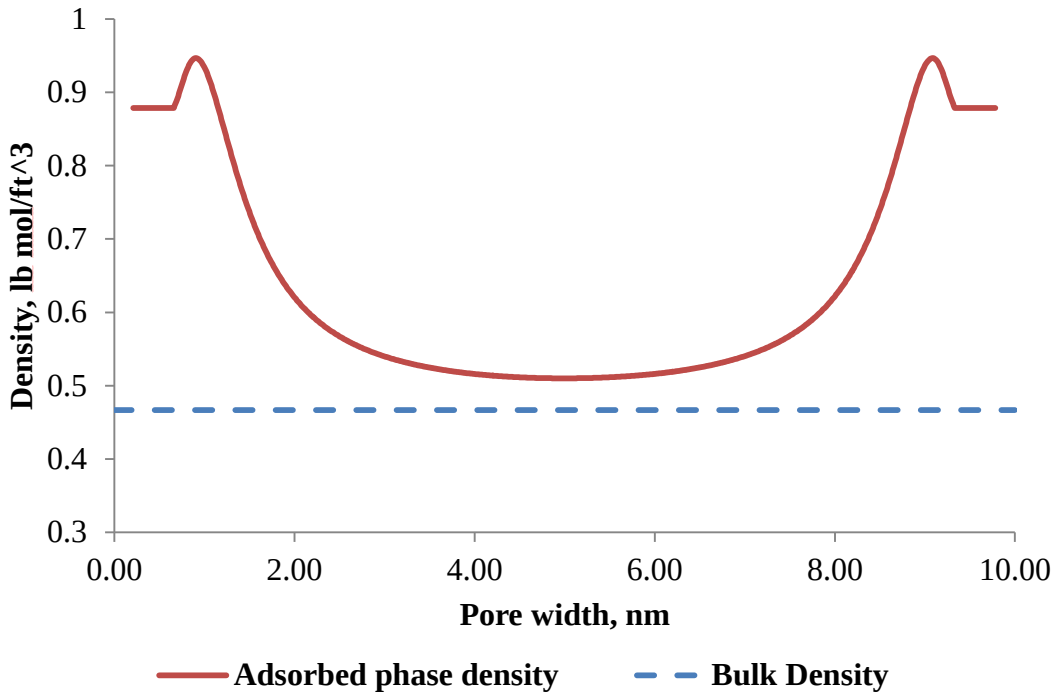


**Figure 3.4 — Fluid density distribution of a multicomponent mixture consisting of 40% methane, 30% ethane, 20% propane, and 10% butane for a 10 nm cylindrical pore at a pressure of 3000 psia and temperature of 300°F**

| **Table 3.2—Compares the Average Adsorbed Phase Density Across a 10 nm Pore with the Bulk Density Value Evaluated at a Pressure of 3000 psia and Temperature of 300°F** | |
|---|---|
| Bulk Density, lb mol/ft$^3$ | 0.467 |
| Average Adsorbed Phase Density, lb mol/ft$^3$ | 0.647 |
| Percentage difference | 28% |

From **Figure 3.4** it is clear that density distribution under confinement effects approaches the bulk density value near the center region of the pore. In contrast, as one moves closer to the wall, the density distribution deviates further from the bulk density value. The resulting density distribution with higher density near the pore walls and lower density near the center of the pore can be explained by analyzing the system on a

molecular level. Hence, we will investigate compositional distributions within the 10 nm pore space for the fluid mixture at identical pressure and temperature conditions. **Figure 3.5** shows the compositional distributions within the 10 nm pore space for the multicomponent gas mixture being studied.

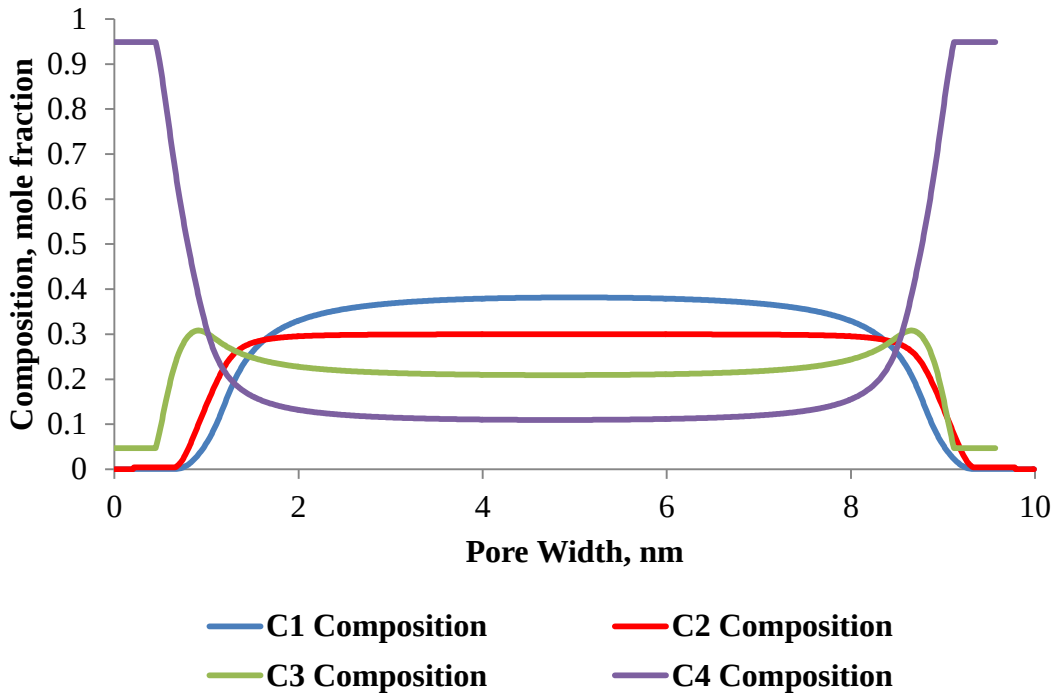


**Figure 3.5 — Compositional distributions across a 10 nm pore for a four component mixture containing methane, ethane, propane, and butane at a pressure of 3000 psia and temperature of 300°F**

Analyzing **Figure 3.5**, it is obvious that the composition of each component varies throughout the pore space. The heavier or larger components dominate along the pore wall and the lighter or smaller components approach their peak value near the center of the pore. **Figure 3.6-3.9** shows the compositional distribution for each component

(methane, ethane, propane, and butane) within the 10 nm pore space. Further each figure compares the compositional distribution to its bulk state composition.

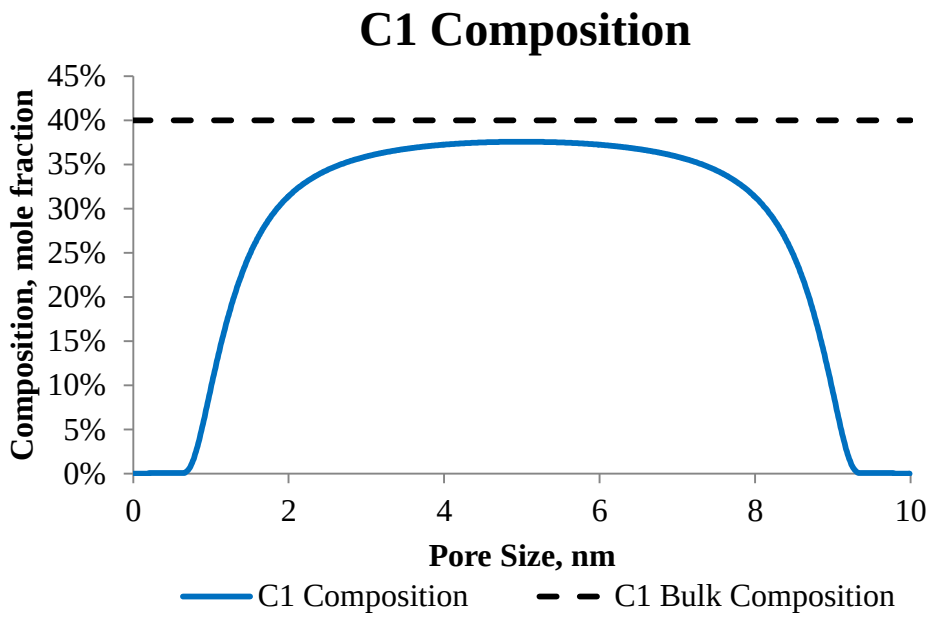


**Figure 3.6 — Compares the compositional distribution of methane within the 10 nm pore under confinement effects to the bulk phase composition**

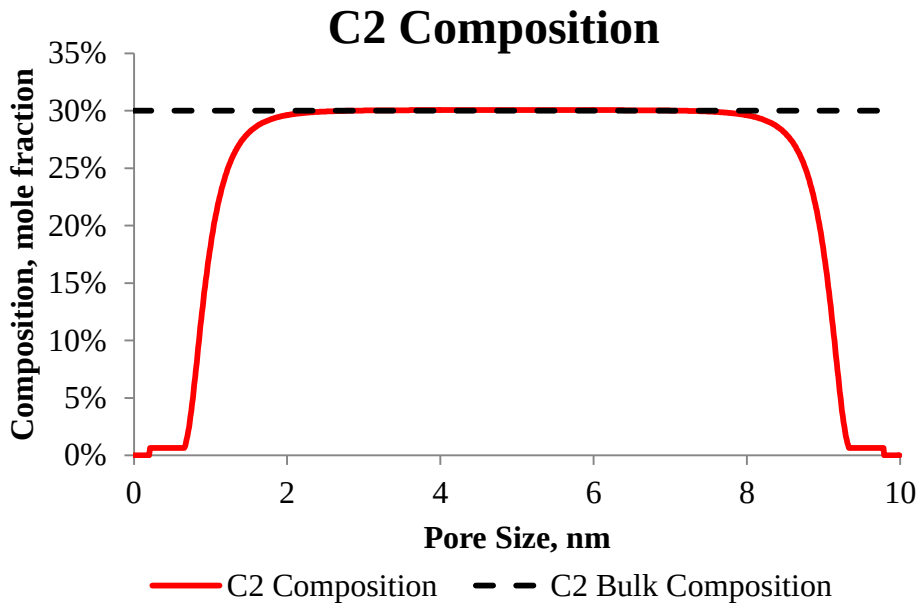


**Figure 3.7 — Compares the compositional distribution of ethane within the 10 nm pore under confinement effects to the bulk phase composition**

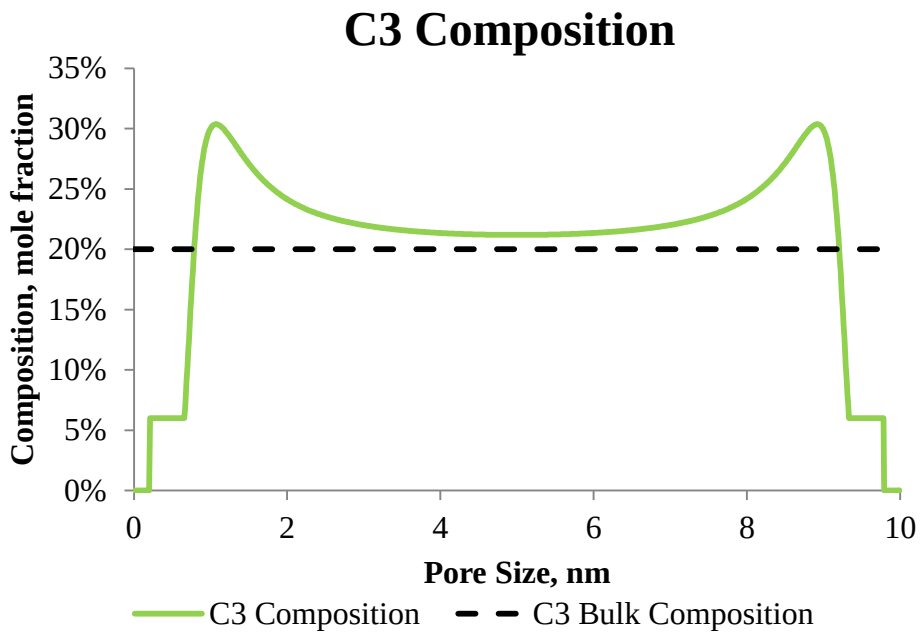


**Figure 3.8 — Compares the compositional distribution of propane within the 10 nm pore under confinement effects to the bulk phase composition**

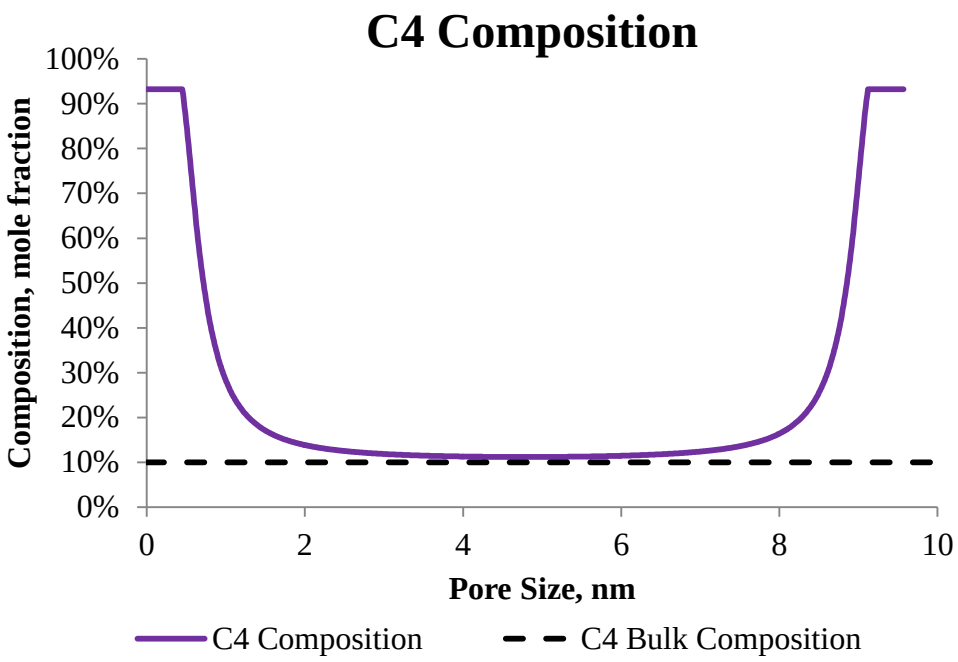


**Figure 3.9 — Compares the compositional distribution of butane within the 10 nm pore under confinement effects to the bulk phase composition**

**Figures 3.6-3.9** suggests that the overall size of the hydrocarbon molecule has a significant influence on its adsorption potential. Note that the composition of butane, i.e. the largest component in the mixture, varies between 10% and 93%. The composition of methane, i.e. the smallest component in the mixture, varies between 0% and 38%. Under confinement conditions, the larger the molecule, the greater its propensity it is to be in the adsorbed state. One of the main causes of this is the presence of Van der Waals forces. Van der Waals forces are the weakest of all intermolecular forces and result from individual electrostatic attractions between molecules. Van der Waals forces arise because of the unsymmetrical electron distribution among molecules. The unsymmetrical distribution of electrons induces a dipole on neighboring molecules

or surfaces resulting in a weak bonding force, known as the Van der Waals force. The strength of Van der Waals forces varies considerably with the size and shape of a molecule. The greater number of electrons a molecule possess and the more surface area over which the electrons are allowed to travel, the bigger the induced dipole becomes. This results in a stronger Van der Waals force. Larger molecules have a greater number of electrons and a larger radius, thus they exhibit stronger Van der Waals forces. Because larger molecules exhibit greater temporary dipoles, these molecules are considered to be "stickier" and have a tendency to form along the pore wall in the adsorbed phase region. This concept is justified by the compositional distributions presented by our analysis. As seen in **Figure 3.6**, as one approaches the wall, the methane composition drops dramatically, approaching zero. When the methane composition of the mixture becomes negligible, the fluid composition becomes dominated by butane along the pore wall as shown in **Figure 3.9**. Another observation that can be made from **Figures 3.6**-**3.9** is that as one approaches the center region of the pore space, the composition of each component approaches its bulk phase composition. This means as one moves toward the center of the pore space, the influence of the fluid-solid interactions becomes minimized and the fluid density approaches its bulk phase density. Compositional distributions for a five component mixture and a six component mixture at identical pressure and temperature conditions are given below:

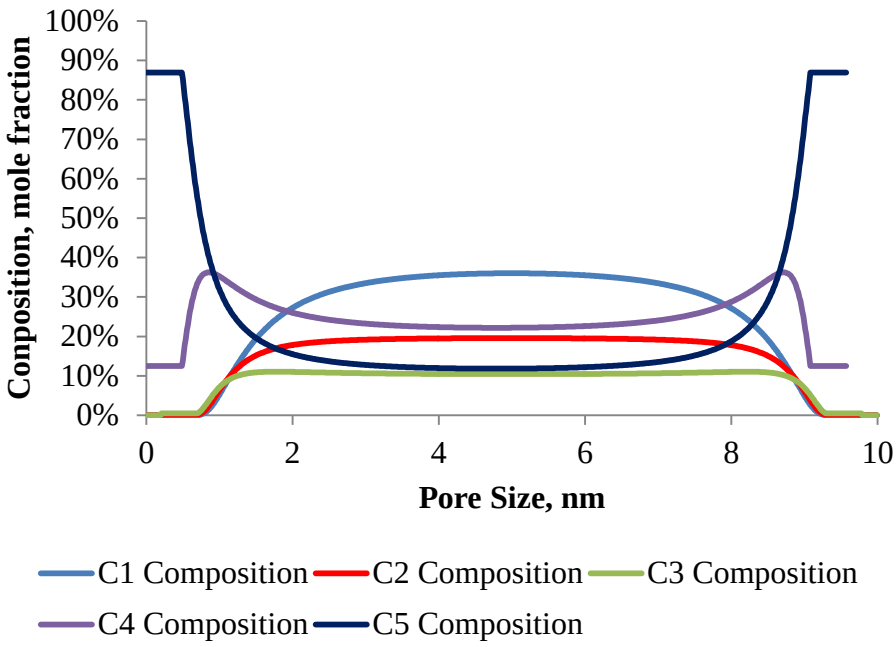


**Figure 3.10 — Compositional distributions across a 10 nm pore for a five component mixture containing methane, ethane, propane, butane, and pentane at a pressure of 3000 psia and temperature of 300°F**

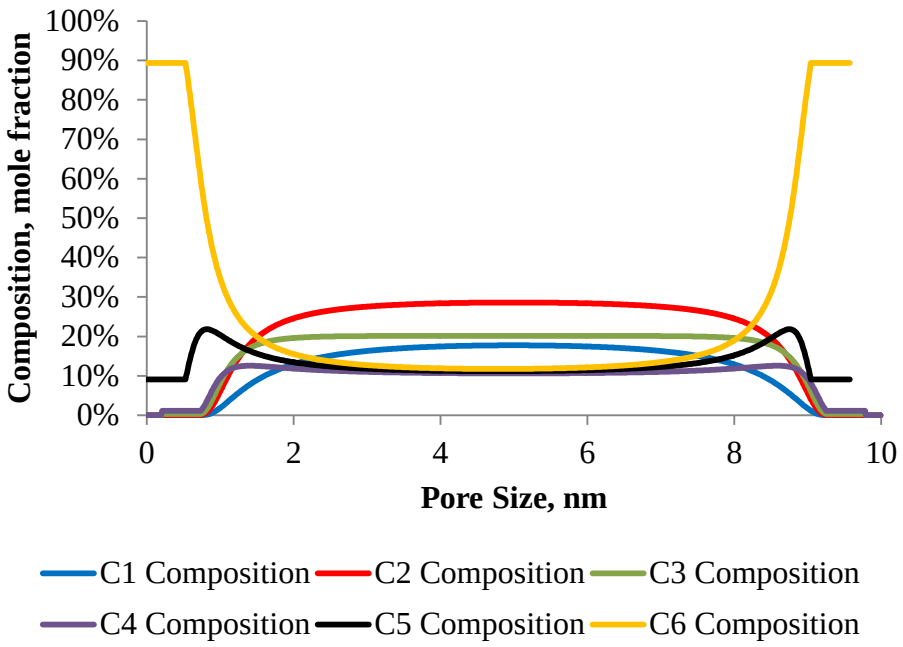


**Figure 3.11 — Compositional distributions across a 10 nm pore for a six component mixture containing methane, ethane, propane, butane, pentane, and hexane at a pressure of 3000 psia and temperature of 300°F**

In **Figures 3.10-3.11**, similar trends can be observed. As heavier components are introduced to the system, the compositional distributions are altered along the pore wall. The smaller, low molecular weight molecules are replaced by the larger, high molecular weight molecules along the adsorbent surface.

## 3.3 Macroscopic Level: Multicomponent Shale Gas in Place Calculations with Adsorbed-Phase Considerations

### *3.3.1 Langmuir Monolayer Adsorption and SLD-PR EOS Comparisons*

In the previous section, we applied the cylindrical form of the SLD-PR EOS algorithm to model the compositional distribution of components within a cylindrical pore of a multicomponent gas mixture. We were able to enhance our understanding on how the fluid molecules interact in a confined environment. In this section, we calculated the adsorbed gas volume, free gas volume, and total gas volume of a multicomponent mixture using the SLD-PR EOS cylindrical model. We compared the results against the Langmuir monolayer adsorption model outlined in Chapter 2. To compare the variance in OGIP values between the two different calculation procedures, a multicomponent mixture with the following composition and thermodynamic properties shown in the **Table 3.3** below was evaluated across a wide pressure range (1,000 to 10,000 psi) at a reservoir temperature of 270 °F. The core data and OGIP calculation parameters are given in **Table 3.3**. **Table 3.4** shows the petrophysical measurements derived from the Barnett core sample.

| Table 3.3—Multicomponent Mixture Composition and Thermodynamic Properties | | | | | | |
|---|---|---|---|---|---|---|
| **Component** | **Bulk Composition ($Z_i$)** | **Critical Pressure ($P_C$), psia** | **Critical Temperature (TC), °R** | **Acentric Factor (Ꞷ)** | **$\sigma_{ff}$** | **$\epsilon_{fs}$** |
| $C_1$ | 61.9% | 669 | 343 | 0.011 | 0.376 | 149 |
| $C_2$ | 14.1% | 709 | 550 | 0.099 | 0.444 | 216 |
| $C_3$ | 8.4% | 618 | 666 | 0.152 | 0.512 | 237 |
| $C_4$ | 4.4% | 552 | 765 | 0.200 | 0.469 | 531 |
| $C_5$ | 2.3% | 490 | 845 | 0.252 | 0.578 | 341 |
| $C_6$ | 9.0% | 440 | 914 | 0.300 | 0.595 | 399 |

| Table 3.4—Langmuir and SLD-PR EOS Calculation Parameters | | |
|---|---|---|
| **Parameters** | **Values** | **Units** |
| Total Porosity, $\phi_T$ | 5.5% | |
| Kerogen Porosity (organic) | 3.5% | |
| Inorganic Porosity | 2.0% | |
| Water Saturation, $S_w$ | 25% | |
| Rock density | 2.5 | g/cm3 |
| Langmuir storage capacity ($G_{sL}$) | 20 | scf/ton |
| Langmuir Pressure ($P_L$) | 1500 | psia |

Using the pore size distribution in **Figure 2.5** and the parameters in **Tables 3.3 and 3.4**, the total gas storage capacity calculated for the gas mixture at different pressures using the two separate methods is presented in **Figure 3.12**. The gas storage values were converted to units of scf/ton.

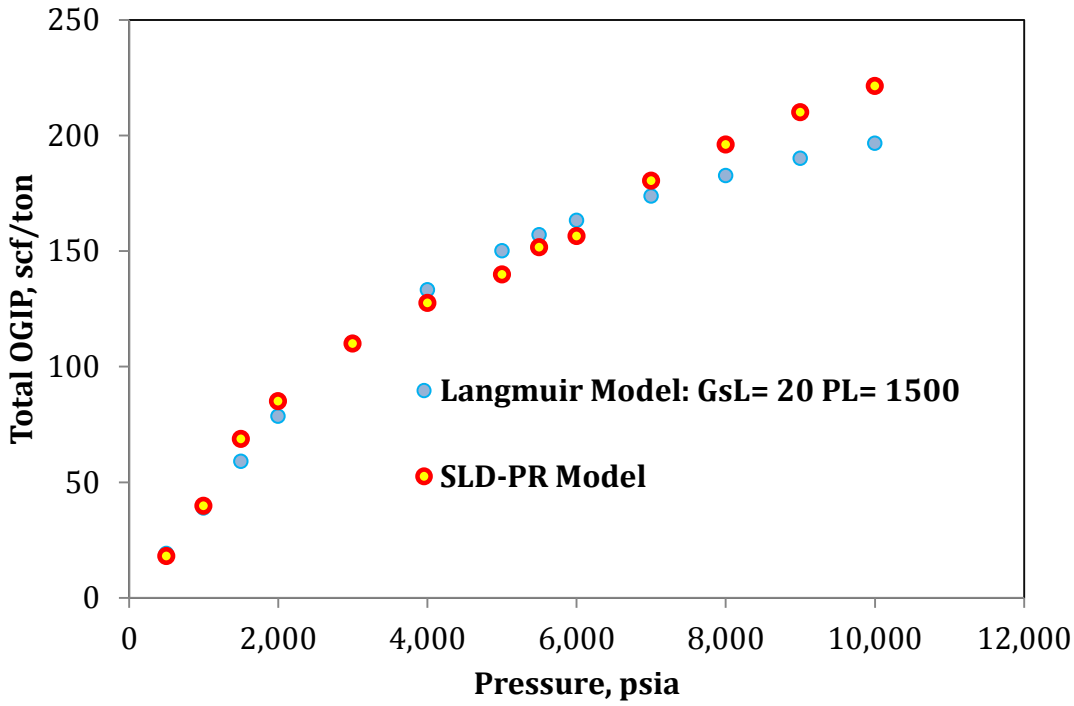


**Figure 3.12—Total gas storage capacity calculated values using the two separate calculation procedures for multicomponent mixtures**

For this particular case, the estimated total gas volumes from these two algorithms are similar below a pressure of 7000 psia. The model predicted values begin to deviate more as pressure increases beyond 7000 psia as shown by the trend. Though the differences look insignificant from a total gas storage perspective, the free gas and adsorbed gas volume values differentiate significantly. The adsorbed gas storage capacity calculated for the gas mixture at different pressures using the two separate methods is presented in **Figure 3.13**. The percentage difference between adsorbed gas storage values is shown in **Figure 3.14**.

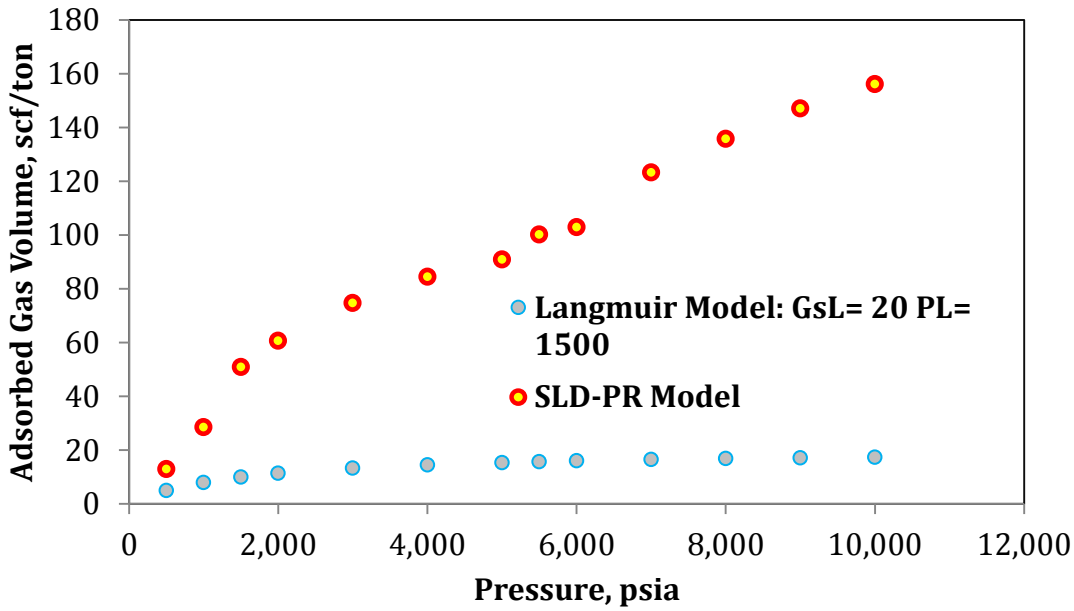


**Figure 3.13 — Adsorbed gas storage capacity calculated values using the two separate methods for a multi-component mixture**

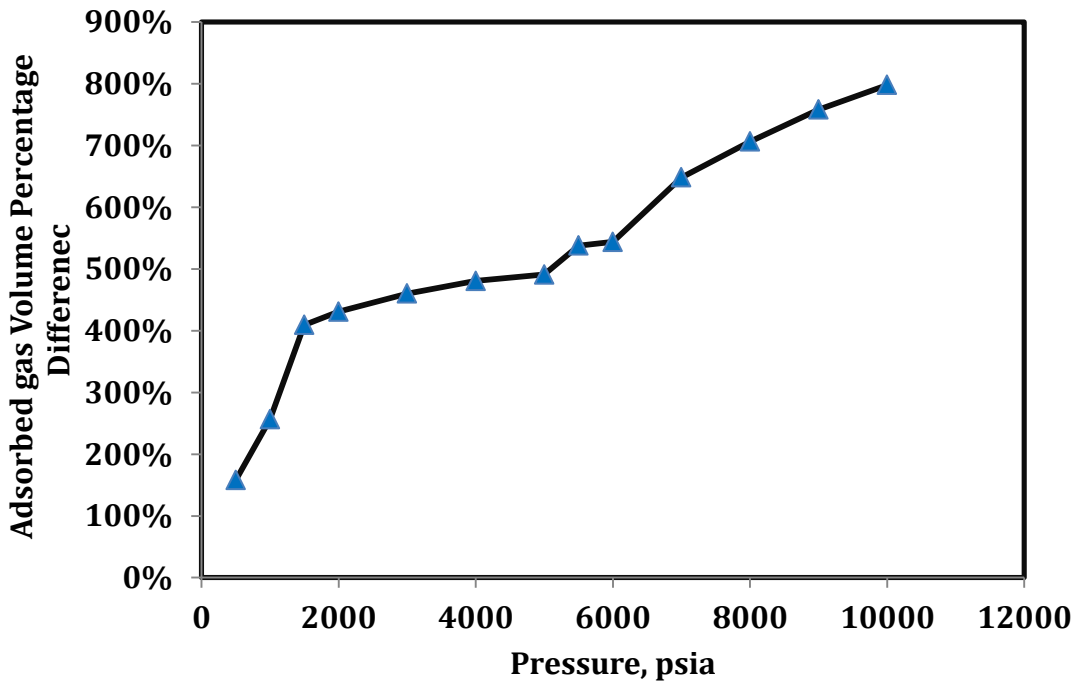


**Figure 3.14 — Adsorbed gas volume percentage difference based on the values calculated in Figure 3.13**

The results suggest the Langmuir model severely underestimates the adsorbed gas storage capacity, especially at high pressures. **Figure 3.13** suggests the percentage difference between the adsorbed gas volume values for the Langmuir isotherm equation and SLD-PR EOS model increases with increasing pressure for the multicomponent mixture. It is clear from **Figure 3.14** that the largest percentage error between the two models occurs at a reservoir pressure of 10,000 psia. The error exceeds 800%. Explanations for such large error can be attributed to the assumptions that go into the Langmuir isothermal equation and lab measuring and reporting techniques. For instance, Das, Jonk, and Schelble (2012) studied the data variability of Langmuir sorption and measuring techniques by sending similar core samples to four vendors.

They reported that three of four vendors conducted sorption measurements much below the saturation point of the gas and in-situ reservoir pressure. Das, Jonk, and Schelble (2012) declared that the extrapolation to higher pressures would produce erroneous results for adsorbed gas volume values calculated by the Langmuir isothermal equation. Either way the adsorbed gas volume values calculated by the two methods disagree with each other significantly at each pressure.

The free gas storage capacity calculated for the gas mixture at different pressures using the two separate methods is presented in the **Figure 3.15**.

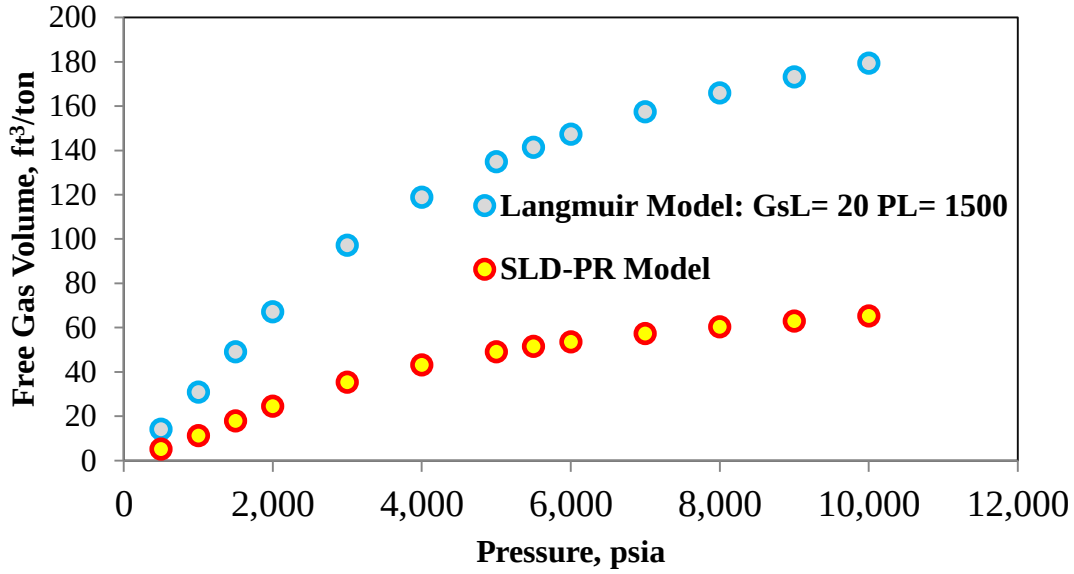


**Figure 3.15 — Free gas storage capacity calculated values using the two separate methods for a multi-component mixture**

The results from **Figure 3.15** suggest that the Langmuir model predicts much higher free gas volume values than the SLD-PR EOS calculation procedure. For each pressure value, the Langmuir calculation procedure predicts a free gas volume that is 64% higher

than the SLD-PR EOS model. This difference in values can be attributed to the calculation procedure illustrated in **Figure 2.8**. The Langmuir calculation procedure associates the free gas volume with the entire pore space where as the new proposed method may or may not include free gas volume in the organic pore space. The amount of free gas in the organic pore space depends on the amount adsorbed according to the new proposed method. Because of this fact, the Langmuir free gas volume predictions will always be overinflated.

*3.3.2 Pore Size Distribution Sensitivity Study*

In the following sensitivity study we will use the same multicomponent mixture and thermodynamic properties given in **Table 3.3**. In addition we will assume a reservoir temperature of 270°F and use the same inorganic and organic porosity values given in **Table 3.4**. Four case studies were evaluated using the gamma distribution. A summary of the gamma distribution parameters and meaningful statistics are presented in **Table 3.5**. The pore size distributions and pore volume contribution by pore size for each case are given in **Figures 3.16-3.19**.

**Table 3.5 — Gamma Distribution and Statistical Parameters**

| Case | k | θ | $\mu_{mean}$, nm | $\sigma_{std}$, nm |
|---|---|---|---|---|
| Case 1 | 0.5 | 5 | 2.5 | 3.5 |
| Case 2 | 1 | 5 | 5 | 5.0 |
| Case 3 | 3 | 5 | 15 | 8.7 |
| Case 4 | 8 | 5 | 40 | 14.1 |

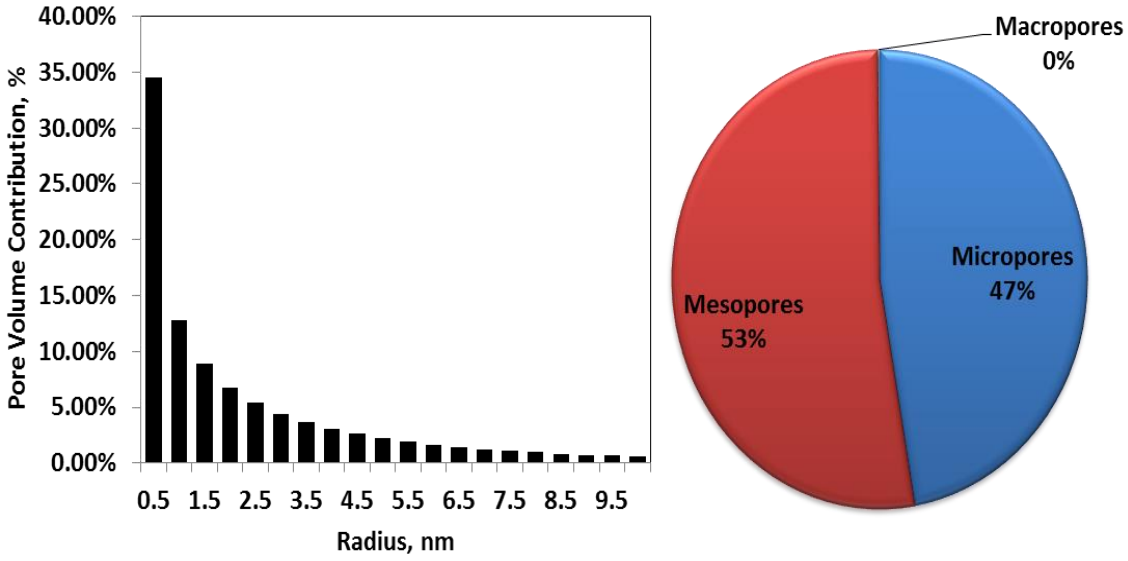


**Figure 3.16 — Pore volume distribution for Case 1**

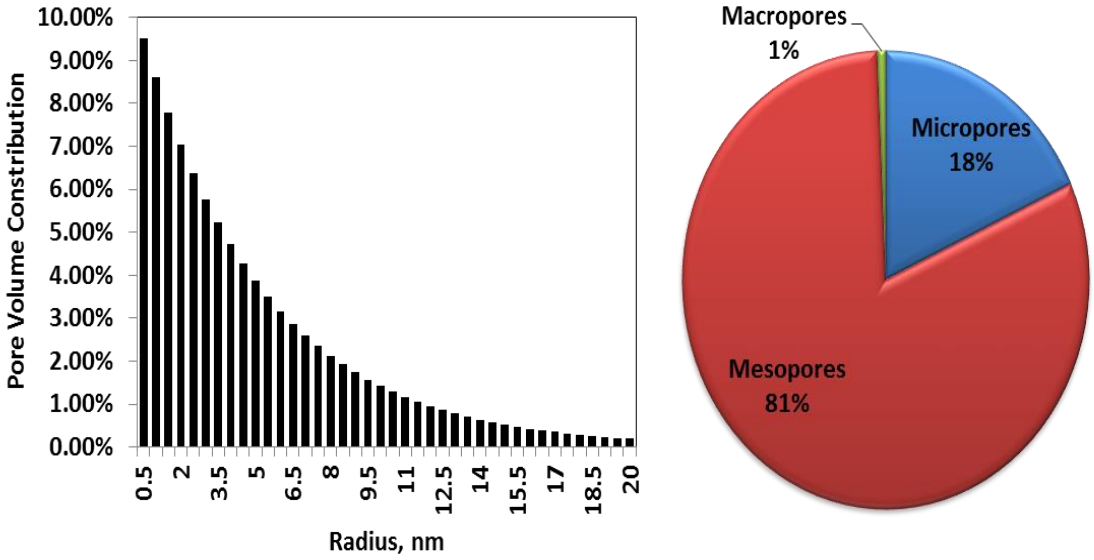


**Figure 3.17— Pore volume distribution for Case 2**

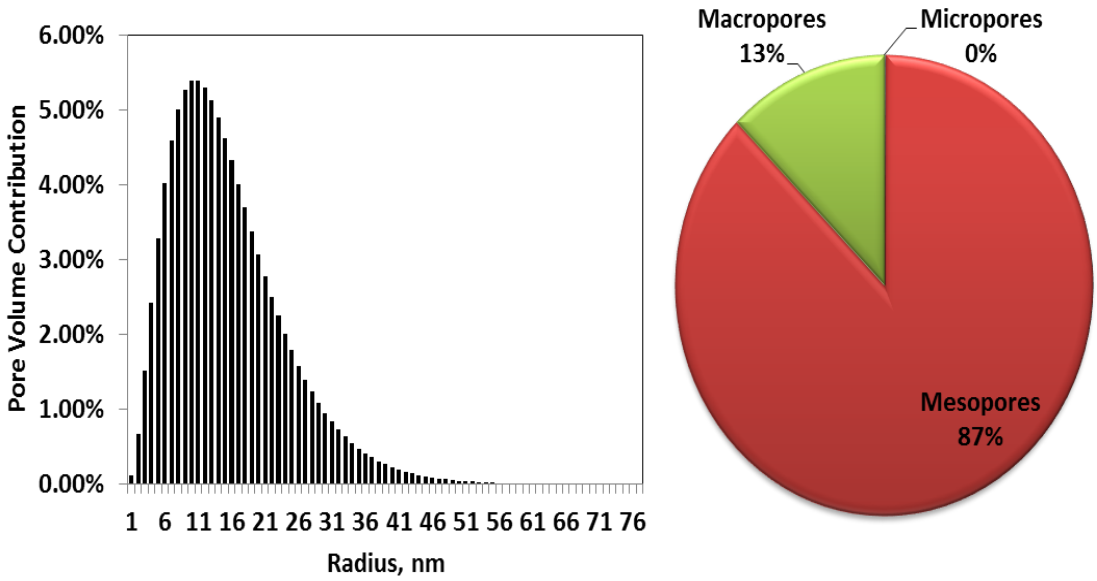


**Figure 3.18 — Pore volume distribution for Case 3**

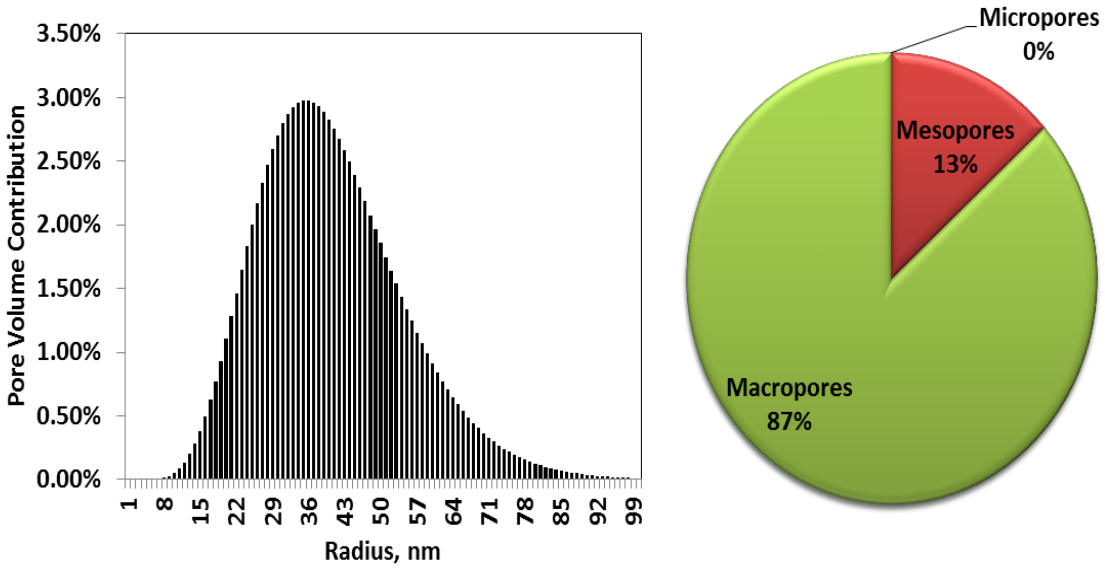


**Figure 3.19 — Pore volume distribution for Case 4**

Comparing **Figures 3.16-3.19**, we observe a significant difference between the pore volume contributions from micropores, mesopores, and macropores. For Case 1, micropores contribute to 47% of the total pore volume and there is no macropore

contribution. For Case 2, only 18% of the pore volume is represented by micropores. For Case 3, the pore volume contribution from the micropores is exactly zero. For Case 4, the pore volume contribution is dominated by the macropores, contributing to exactly 87% of the total pore volume. It is immediately apparent that Cases 1-4 simulate a wide range of pore size distributions that a gas shale core might exhibit. To further assess the importance of pore size distribution in shale gas reservoirs, OGIP values were calculated using the same SLD-PR EOS procedure illustrated in **Figure 2.8** and core data in **Table 3.4** for a wide range of reservoir pressures. The results are given in the **Figure 3.20**.

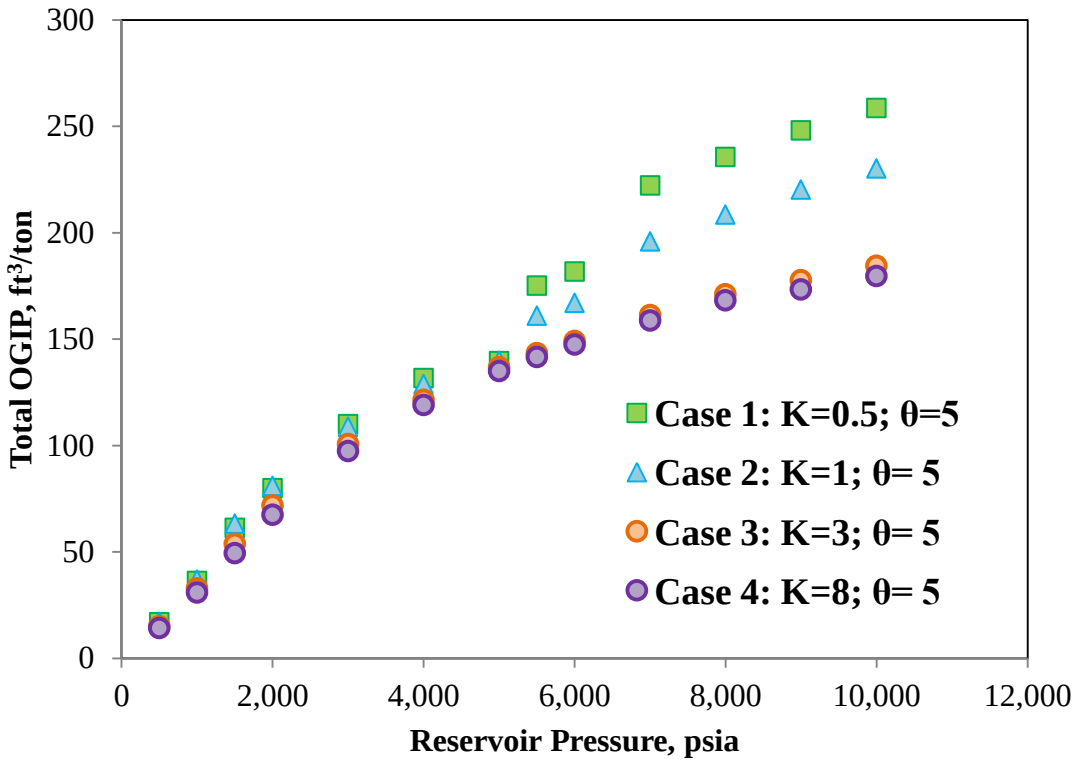


**Figure 3.20— OGIP values for Cases 1-4 across a wide pressure range**

**Figure 3.20** suggests for identical pore volumes evaluated at the same pressure and temperature conditions, more small pores correlates to more gas in place, especially at increasing pressures. Thus under a similar depletion process, one would expect higher gas recovery from smaller pores. It is clear from **Figure 3.20** that the largest percentage difference between the calculated OGIP values occurs at a reservoir pressure of 10,000 psia between Case 1 and Case 4. The percentage error is 43.9%. Another observation from **Figure 3.20** is as the pore contribution from macropores increases, the influence of pore size distribution on OGIP values becomes less significant. As shown in **Figure 3.21**, as the percentage of macropores increases in a sample, the average density of the pore size distribution begins to approach the bulk density, i.e. the density at which pore wall effects are not an influence. This is especially true for cases 3 and 4.

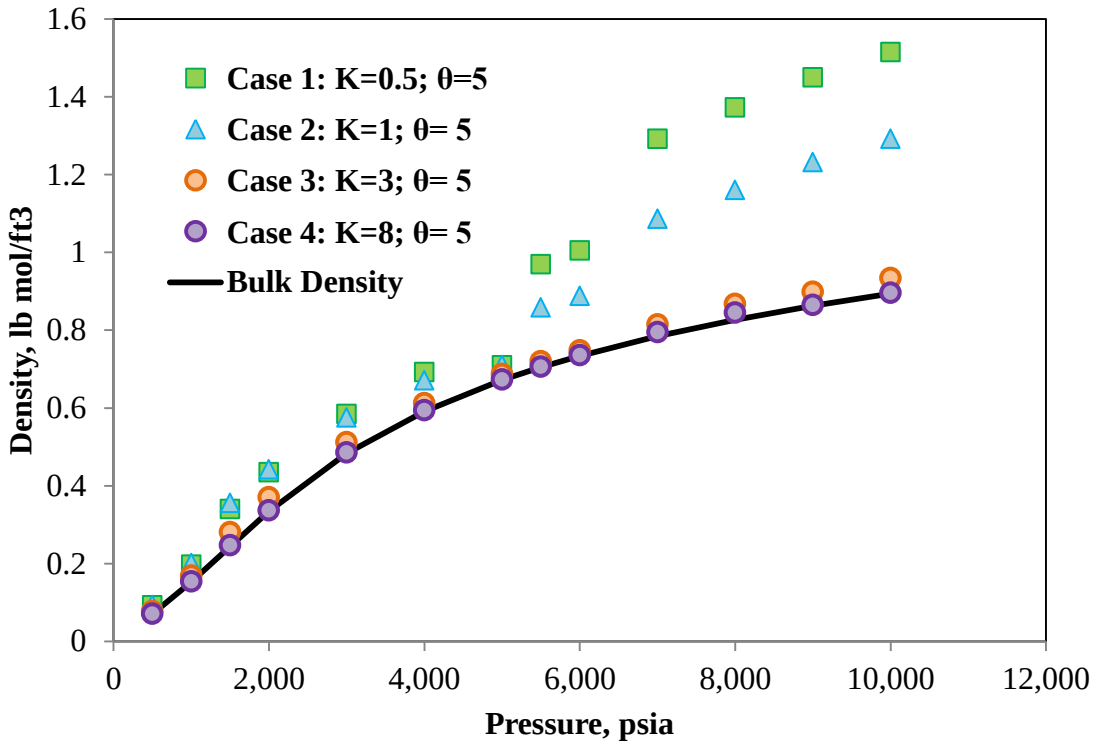


**Figure 3.21 — Average pore size distribution densities for Cases 1 through 4 and bulk density values across a wide range of pressures**

From the results presented in **Figure 3.20** it becomes immediately apparent of the significance of pore size distribution on OGIP values in shale gas reservoirs when a large percentage of the pore volume consists of micropores and mesopores. When you consider multiple samples with identical pore volumes and different pore size distributions as done here there are a couple of considerations that can be taken into account. The first consideration is the pore volume contribution of smaller pores. The adsorbed layer density increases in smaller pores due to the fluid-wall interactions, thus resulting in more gas in place. Another consideration is surface area. The capacity of adsorbed material scales directly with the surface area of the pore walls when pore

volumes are identical. Given the potential impact of micropore effects on adsorption storage capacities of shale gas samples, consideration of pore size distributions is very important for OGIP studies and predictions.

## Chapter 4: Conclusions

This work investigates multicomponent adsorption on a nanoscopic, molecular, and macroscopic level in gas shale reservoirs by applying the cylindrical form of the SLD-PR EOS model. The following conclusions were derived from this work:

1. In a confined environment, the adsorbed phase density is influenced by pore size, temperature, and pressure. The adsorbed phase density increases with decreasing pore size and decreases with increasing temperature. Further, the adsorbed phase density increases with increasing pressure until all adsorption sites are filled. Once all the adsorption sites are filled, adsorption no longer occurs.
2. The overall size of an organic molecule has a significant effect on its adsorption potential. When a fluid contains many components, the larger molecules have a tendency to occupy the majority of the pore space along the pore wall.
3. A new calculation procedure using the cylindrical Simplified Local Density model with Peng-Robinson Equation of State (SLD-PR EOS) is proposed to replace the Langmuir isotherm-based monolayer adsorption model. The proposed method respects the dual porosity system of organic rich shale and is based on the fundamentals of chemical potential equilibrium.
4. The presence of micropores in shales is associated with more gas in place when pore volumes are identical.

5. Pore size distribution has a tremendous impact on gas volume in a shale formation, and neglecting pore size distribution can yield more than 44% errors for original gas in place (OGIP) calculation.

Future work will consider verifying the density profiles from the SLD-PR multicomponent cylindrical model with molecular dynamic simulation.

## References


1. Adesida, A.G., Akkutlu, I., Resasco, D.E. et al. 2011. Characterization of Barnett Shale Kerogen Pore Size Distribution using DFT Analysis and Grand Canonical Monte Carlo Simulations. Presented at the SPE Annual Technical Conference and Exhibition, Denver, Colorado, 30 October-2 November. SPE-147397-MS. http://dx.doi.org.ezproxy.lib.ou.edu/10.2118/147397-MS.

2. Al Ismail, M. and Horne, R.N. 2014. Modeling Adsorption of Gases in Nanoscale Pores Using Grand Canonical Monte Carlo Simulation Techniques. Presented at the SPE Annual Technical Conference and Exhibition, Amsterdam, The Netherlands, 27-29 October. SPE-170948-MS. http://dx.doi.org.ezproxy.lib.ou.edu/10.2118/170948-MS.

3. Alder, B.J. and Wainwright, T.E. 1959. Studies in Molecular Dynamics. I. General Method. *The Journal of Chemical Physics* **31** (2): 459-466. http://scitation.aip.org/content/aip/journal/jcp/31/2/10.1063/1.1730376.

4. Ambrose, R.J., Hartman, R.C., Diaz-Campos, M. et al. 2012. Shale Gas-in-Place Calculations Part I: New Pore-Scale Considerations. *SPE J.* **17** (01): 219 - 229. SPE-131772-PA. http://dx.doi.org.ezproxy.lib.ou.edu/10.2118/131772-PA.

5. Appelo, C.A.J., Hendriks, J.A., and van Veldhuizen, M. 1993. Flushing factors and a sharp front solution for solute transport with multicomponent ion exchange. *Journal of Hydrology* **146**: 89-113. http://www.sciencedirect.com/science/article/pii/002216949390271A.

6. Bowker, K.A. 2007. Development of the Barnett Shale Play, Fort Worth Basin. *West Texas Geological Society* **42** (6): 4-11.

7. Bruner, K.R. and Smosna, R. 2011. A Comparitive Study of the Mississippian Barnett Shale, Fort Worth Basin, and Devonian Marcellus Shale, Appalachian Basin, URS Corporation, San Francisco, CA (April 2011).

8. Cananaugh, T. and Wallis, J.D. 2015. Multi-Resolution Imaging of Shales Using Electron and Ion Microscopy. Presented at the Unconventional Resources Technology Conference (URTeC), San Antonio, Texas. 10.15530/urtec-2015-2154620.

9. Chen, J. 2005. Simplified Local-Density Modeling of Pure and Multi-Component Gas Adsorption on Dry and Wet Coals. Master of Science, Oklahoma State University, Stillwater, OK (December, 2007).

10. Chen, J.H., Wong, D.S.H., Tan, C.S. et al. 1997. Adsorption and Desorption of Carbon Dioxide onto and from Activated Carbon at High Pressures. *Industrial & Engineering Chemistry Research* **36** (7): 2808-2815. http://dx.doi.org/10.1021/ie960227w.

11. Clarkson, C.R. and Bustin, R.M. 1999. The effect of pore structure and gas pressure upon the transport properties of coal: a laboratory and modeling study. 2. Adsorption rate modeling. *Fuel* **78** (11): 1345-1362. http://www.sciencedirect.com/science/article/pii/S0016236199000563.

12. Conn, A., Gould, N., and Toint, P. 2000. *Trust Region Methods*. Philadelphia, PA: Society for Industrial and Applied Mathematics.

13. Curtis, M.E., Ambrose, R.J., and Sondergeld, C.H. 2010. Structural Characterization of Gas Shales on the Micro- and Nano-Scales. Presented at the Canadian Unconventional Resources and International Petroleum Conference, Calgary, Alberta, Canada, 19-21 October. SPE-137693-MS. http://dx.doi.org.ezproxy.lib.ou.edu/10.2118/137693-MS.

14. Curtis, M.E., Ambrose, R.J., Sondergeld, C.H. et al. 2011. Investigation of the Relationship Between Organic Porosity and Thermal Maturity in The Marcellus Shale. Presented at the North American Unconventional Gas Conference and Exhibition, The Woodlands, Texas, 14-16 June. http://dx.doi.org.ezproxy.lib.ou.edu/10.2118/144370-MS.

15. Das, M., Jonk, R., and Schelble, R. 2012. Effect Of Multicomponent Adsorption/Desorption Behavior On Gas-In-Place (GIP) and Estimated Ultimate Recovery (EUR) In Shale Gas Systems. Presented at the SPE Annual Technical Conference and Exhibition, San Antonio, Texas, 8-10 October. SPE-159558-MS. http://dx.doi.org.ezproxy.lib.ou.edu/10.2118/159558-MS.

16. Devegowda, D., Sapmanee, K., Civan, F. et al. 2012. Phase Behavior of Gas Condensates in Shales Due to Pore Proximity Effects: Implications for Transport, Reserves and Well Productivity. Presented at the SPE Annual Technical Conference and Exhibition, San Antonio, Texas, 8-10 October. http://dx.doi.org.ezproxy.lib.ou.edu/10.2118/160099-MS.

17. Dhanapal, K., Devegowda, D., Zhang, Y. et al. 2014. Phase Behavior and Storage in Organic Shale Nanopores: Modeling of Multicomponent Hydrocarbons in Connected Pore Systems and Implications for Fluids-in-place Estimates in Shale Oil and Gas Reservoirs. Presented at the SPE Unconventional Resources Conference, The Woodlands, Texas, 1-3 April. SPE-169008-MS. http://dx.doi.org.ezproxy.lib.ou.edu/10.2118/169008-MS.

18. Diaz Campos, M., Akkutlu, I.Y., and Sigal, R.F. 2009. A Molecular Dynamics Study on Natural Gas Solubility Enhancement in Water Confined to Small Pores. Presented at the SPE Annual Technical Conference and Exhibition, New Orleans, Louisiana 2009/1/1/. http://dx.doi.org.ezproxy.lib.ou.edu/10.2118/124491-MS.

19. DOE, U. 2009. *Modern Shale Gas Development in the United States* (Reprint).

20. Dong, T., Harris, N.B., Ayranci, K. et al. 2015. Porosity characteristics of the Devonian Horn River shale, Canada: Insights from lithofacies classification and shale composition. *International Journal of Coal Geology* **141–142** (0): 74-90. http://www.sciencedirect.com/science/article/pii/S0166516215000336.

21. Driskill, B., Walls, J., Sinclair, S.W. et al. 2013. Micro-scale Characterization of the Eagle Ford Formation Using SEM Methods and Digital Rock Modeling. Presented at the Unconventional Resources Technology Conference, Denver, Colorado, 12-14 August. http://dx.doi.org.ezproxy.lib.ou.edu/10.1190/URTEC2013-165.

22. Erto, A., Lancia, A., and Musmarra, D. 2011. A modelling analysis of PCE/TCE mixture adsorption based on Ideal Adsorbed Solution Theory. *Separation and Purification Technology* **80** (1): 140-147. http://www.sciencedirect.com/science/article/pii/S1383586611002450.

23. Fitzgerald, J.E., Sudibandriyo, M., Pan, Z. et al. 2003. Modeling the adsorption of pure gases on coals with the SLD model. *Carbon* **41** (12): 2203-2216. http://www.sciencedirect.com/science/article/pii/S0008622303002021.

24. Frenkel, D. and Smit, B. 2001. *Understanding Molecular Simulation : From Algorithms to Applications*. Amsterdam, NLD: Academic Press.

25. Hartman, R.C., Ambrose, R.J., Akkutlu, I.Y. et al. 2011. Shale Gas-in-Place Calculations Part II - Multicomponent Gas Adsorption Effects. Presented at the

North American Unconventional Gas Conference and Exhibition, The Woodlands, Texas, 14-16 June. http://dx.doi.org.ezproxy.lib.ou.edu/10.2118/144097-MS.

26. Honarpour, M.M., Nagarajan, N.R., Orangi, A. et al. 2012. Characterization of Critical Fluid PVT, Rock, and Rock-Fluid Properties - Impact on Reservoir Performance of Liquid Rich Shales. Presented at the SPE Annual Technical Conference and Exhibition, San Antonio, Texas, 8-10 October. http://dx.doi.org.ezproxy.lib.ou.edu/10.2118/158042-MS.

27. Jin, L., Ma, Y., and Jamili, A. 2013. Investigating The Effect of Pore Proximity on Phase Behavior And Fluid Properties in Shale Formations. Presented at the SPE Annual Technical Conference and Exhibition, New Orleans, Louisiana, 30 September-2 October. SPE-166192-MS. http://dx.doi.org.ezproxy.lib.ou.edu/10.2118/166192-MS.

28. Joshi, A.V. 2011. Statistical Analysis of In-Line Inspection Performance With Gamma Distribution. Presented at the CORROSION 2011, Houston, Texas 13-17 March.

29. Kang, S.M., Fathi, E., Ambrose, R.J. et al. 2011. Carbon Dioxide Storage Capacity of Organic-Rich Shales. *Journal of Petroleum Technology* **63** (07): 114 - 117. http://dx.doi.org.ezproxy.lib.ou.edu/10.2118/0711-0114-JPT.

30. Langmuir, I. 1918. THE ADSORPTION OF GASES ON PLANE SURFACES OF GLASS, MICA AND PLATINUM. *Journal of the American Chemical Society* **40** (9): 1361-1403. http://dx.doi.org/10.1021/ja02242a004.

31. Lipatov, Y., Todosijchuk, T., and Chornaya, V. 1993. Adsorption of Polymer Mixtures from Dilute and Semidilute Solutions. *Journal of Colloid and Interface Science* **155** (2): 283-289. http://www.sciencedirect.com/science/article/pii/S0021979783710374.

32. Luo, S., Lutkenhaus, J.L., and Nasrabadi, H. 2015. Experimental Study of Confinement Effect on Hydrocarbon Phase Behavior in Nano-Scale Porous Media Using Differential Scanning Calorimetry. Presented at the SPE Annual Technical Conference and Exhibition, Houston, Texas, 28-30 September. SPE-175095-MS. http://dx.doi.org.ezproxy.lib.ou.edu/10.2118/175095-MS.

33. Lyklema, J. 2005. Fundamentals of Interface and Colloid Science. **5**: 1-123.

34. Ma, Y. and Jamili, A. 2014a. Modeling the Effects of Porous Media in Dry Gas and Liquid Rich Shale on Phase Behavior. Presented at the SPE Improved Oil Recovery Symposium, Tulsa, Oklahoma, 12-16 April. SPE-169128-MS. http://dx.doi.org.ezproxy.lib.ou.edu/10.2118/169128-MS.

35. Ma, Y. and Jamili, A. 2014b. Using Simplified Local Density/ Peng-Robinson Equation of State to Study the Effects of Confinement in Shale Formations on Phase Behavior. Presented at the SPE Unconventional Resources Conference, SPE Unconventional Resources Conference, 1-3 April. http://dx.doi.org.ezproxy.lib.ou.edu/10.2118/168986-MS.

36. Mayerhofer, M.J., Lolon, E., Warpinski, N.R. et al. 2010. What Is Stimulated Reservoir Volume? **25** (01).

37. McCain, W.D., Jr. 1990. *Properties of Petroleum Fluids (2nd Edition)*, second edition. Tulsa, Oklahoma: PennWell.

38. Menon, P.G. 1968. Adsorption at high pressures. *Chemical Reviews* **68** (3): 277-294. http://dx.doi.org/10.1021/cr60253a002.

39. Michel Villazon, G.G., Sigal, R.F., Civan, F. et al. 2011. Parametric Investigation of Shale Gas Production Considering Nano-Scale Pore Size Distribution, Formation Factor, and Non-Darcy Flow Mechanisms. Presented at the SPE Annual Technical Conference and Exhibition, Denver, Colorado, 30 October-2 November. http://dx.doi.org.ezproxy.lib.ou.edu/10.2118/147438-MS.

40. Mosher, K., He, J., Liu, Y. et al. 2013. Molecular simulation of methane adsorption in micro- and mesoporous carbons with applications to coal and gas shale systems. *International Journal of Coal Geology* **109–110** (0): 36-44. http://www.sciencedirect.com/science/article/pii/S0166516213000049.

41. Myers, A.L. and Prausnitz, J.M. 1965. Thermodynamics of mixed-gas adsorption. *AIChE Journal* **11** (1): 121-127. http://dx.doi.org/10.1002/aic.690110125.

42. Ortiz, V., López-Álvarez, Y.M., and López , G.E. 2005. Phase diagrams and capillarity condensation of methane confined in single- and multi-layer nanotubes. *Molecular Physics* **103** (19): 2587-2592.

43. Ozkan, E. 2014a. *Releasing Shale-Gas Potential with Fractured Horizontal Wells-SPE Distinguished Lecturer* (Reprint).

44. Ozkan, E. 2014b. The Way Ahead for US Unconventional Reservoirs. **10** (03): 37 - 39.

45. Parsa, E., Yin, X., and Ozkan, E. 2015. Direct Observation of the Impact of Nanopore Confinement on Petroleum Gas Condensation. Presented at the SPE Annual Technical Conference and Exhibition, Houston, Texas, 28-30 September. SPE-175118-MS. http://dx.doi.org.ezproxy.lib.ou.edu/10.2118/175118-MS.

46. Peng, B. and Yu, Y.-X. 2008. A Density Functional Theory for Lennard-Jones Fluids in Cylindrical Pores and Its Applications to Adsorption of Nitrogen on MCM-41 Materials. *Langmuir* **24** (21): 12431-12439. http://dx.doi.org/10.1021/la8024099.

47. Petitfrere, M. and Nichita, D.V. 2014. Robust and efficient Trust-Region based stability analysis and multiphase flash calculations. *Fluid Phase Equilibria* **362** (0): 51-68. http://www.sciencedirect.com/science/article/pii/S0378381213004780.

48. Rangarajan, B., Lira, C.T., and Subramanian, R. 1995. Simplified local density model for adsorption over large pressure ranges. *AIChE Journal* **41** (4): 838-845. http://dx.doi.org/10.1002/aic.690410411.

49. Ravikovitch, P.I., Haller, G.L., and Neimark, A.V. 1998. Density functional theory model for calculating pore size distributions: pore structure of nanoporous catalysts. *Advances in Colloid and Interface Science* **76–77** (0): 203-226. http://www.sciencedirect.com/science/article/pii/S0001868698000475.

50. Ravindran, A., Ragsdell, K.M., and Reklaitis, G.V. 2006. *Engineering Optimization: Methods and Applications*, Second Edition edition. Hoboken, New Jersey: John Wiley and Sons.

51. Rezaee, R. 2015. *Fundamentals of Gas Shale Reservoirs*. Hoboken, New Jersey: John Wiley & Sons.

52. Ross, D.J.K. and Marc Bustin, R. 2009. The importance of shale composition and pore structure upon gas storage potential of shale gas reservoirs. *Marine and Petroleum Geology* **26** (6): 916-927. http://www.sciencedirect.com/science/article/pii/S0264817208001153.

53. Saito, A. and Foley, H.C. 1991. Curvature and parametric sensitivity in models for adsorption in micropores. *AIChE Journal* **37** (3): 429-436. http://dx.doi.org/10.1002/aic.690370312.

54. Sigmund, P.M., Dranchuk, P.M., Morrow, N.R. et al. 1973. Retrograde Condensation in Porous Media. *SPJ* **13** (02): 93 - 104.

55. Sing, K.S. 1985. Reporting physisorption data for gas/solid systems with special reference to the determination of surface area and porosity. *Pure and Applied Chemistry* **57**: 603-619.

56. Sondergeld, C.H., Ambrose, R.J., Rai, C.S. et al. 2010. Micro-Structural Studies of Gas Shales. Presented at the SPE Unconventional Gas Conference, Pittsburgh, Pennsylvania, 23-25 February. SPE-131771-MS. http://dx.doi.org.ezproxy.lib.ou.edu/10.2118/131771-MS.

57. Tjatjopoulos, G.J., Feke, D.L., and Mann, J.A. 1988. Molecule-micropore interaction potentials. *The Journal of Physical Chemistry* **92** (13): 4006-4007. http://dx.doi.org/10.1021/j100324a063.

58. Travalloni, L., Castier, M., Tavares, F.W. et al. 2010. Critical behavior of pure confined fluids from an extension of the van der Waals equation of state. *The Journal of Supercritical Fluids* **55** (2): 455-461. http://www.sciencedirect.com/science/article/pii/S0896844610002986.

59. Trebin, F.A. and Zadora, G.I. 1968. Experimental study of the effect of porous media on phase change in gas condensate systems. *Nefti Gaz* **81**: 37.

60. Van Megen, W. and Snook, I.K. 1982. Physical adsorption of gases at high pressure. *Molecular Physics* **45** (3): 629-636. http://dx.doi.org/10.1080/00268978200100481.

61. Wang, L., Neeves, K., Yin, X. et al. 2014. Experimental Study and Modeling of the Effect of Pore Size Distribution on Hydrocarbon Phase Behavior in Nanopores. Presented at the SPE Annual Technical Conference and Exhibition,

Amsterdam, The Netherlands, 27-29 October. SPE-170894-MS. http://dx.doi.org.ezproxy.lib.ou.edu/10.2118/170894-MS.

62. Whiston, C.H. and Brule, M.R. 2000. *Phase Behavior*. Society of Petroleum Engineers.

63. Xu, H., Hjelm, R.P., Ding, M. et al. 2015. Probing Hydrocarbon Fluid Behavior in Shale Formations. Presented at the Unconventional Resources Technology Conference (URTeC), San Antonio, Texas, 20 - 22 July 2015. DOI 10.15530/urtec-2015-2174025.

64. Zarragoicoechea, G.J. and Kuz, V.A. 2004. Critical shift of a confined fluid in a nanopore. *Fluid Phase Equilibria* **220** (1): 7-9. http://www.sciencedirect.com/science/article/pii/S037838120400127X.

65. Zeigermann, P., Dvoyashkin, M., Valiullin, R. et al. 2009. Assessing the Pore Critical Point of the Confined Fluid by Diffusion Measurement. *diffusion-fundamentals.org* **41** (2).

66. Zhang, H., Bai, B., Song, K. et al. 2012. Shale Gas Hydraulic Flow Unit Identification Based on SEM-FIB Tomography. Presented at the SPE Annual Technical Conference and Exhibition, San Antonio, Texas, 8-10 October. http://dx.doi.org.ezproxy.lib.ou.edu/10.2118/160143-MS.